Title
A Proposed Method for the Computer-aided Discovery and Design of High-strength, Ductile Metals

Author
Winter, Ian Stewart

Publication Date
2017

A Proposed Method for the Computer-aided Discovery and Design of High-strength, Ductile Metals

by

Ian Stewart Winter

A dissertation submitted in partial satisfaction of the
requirements for the degree of
Doctor of Philosophy

in

Engineering - Materials Science and Engineering

in the

GRADUATE DIVISION
of the
UNIVERSITY OF CALIFORNIA, BERKELEY

Committee in charge:
Professor Daryl Chrzan, Chair
Professor Mark Asta
Professor Panayiotis Papadopoulos

Spring 2017

A Proposed Method for the Computer-aided Discovery and Design of High-strength, Ductile Metals

Abstract

A Proposed Method for the Computer-aided Discovery and Design of
High-strength, Ductile Metals

by

Ian Stewart Winter
Doctor of Philosophy in Engineering - Materials Science and Engineering

University of California, Berkeley

Professor Daryl Chrzan, Chair

Gum Metal, a class of Ti-Nb alloys, has generated a great deal of interest in the metallurgical community since its development in 2003. These alloys display numerous novel and anomalous properties, many of which only occur after severe plastic deformation has been incurred on the material. Such properties include: superelasticity, super-coldworkability, Invar and Elinvar behavior, high ductility, as well as high strength. The high strength of gum metal has generated particular enthusiasm as it is on the order of the predicted ideal strength of the material. Many of the properties of gum metal appear to be a direct result of tuning the composition to be near an elastic instability resulting in a high degree of elastic anisotropy. This presents an opportunity for the computer-aided discovery and design of structural materials as the ideal strength and elastic anisotropy can be approximated from the elastic constants. Two approaches are described for searching for this high ansitropy. In the first, The possibility of forming gum metal in Mg is explored by tuning the material to be near the BCC-HCP transition either by pressure or alloying with Li. The second makes use of the Materials Project's elastic constants database, which contains thousands of ordered compounds, in order to screen for gum metal candidates. By defining an elastic anisotropy parameter consistent with the behavior of gum metal and calculating it for all cubic materials in the elastic constants database several gum metal candidates are found. In order to better assess their candidacy information on the intrinsic ductility of these materials is necessary. A method is proposed for calculating the ideal strength and deformation mode of a solid solution from first-principles. In order to validate this method the intrinsic ductile-to-brittle transition composition of Ti-V systems is calculated. It is further shown that this method can be applied to the calculation of an ideal tensile yield surface.

To my family

Contents

List of Figures

List of Tables

I would like to begin by expressing my gratitude to my adviser, Daryl Chrzan, for his guidance, teaching, and constant questioning of my results and ideas, as well as for his willingness to take a chance on me in the first place. I would also like to thank the members of my dissertation committee, Professors Mark Asta and Panayiotis Papadopoulos, as well as the other members of my qualifying exam committee, Professors Andrew Minor and Kristin Ceder-Persson, for their helpful comments and thorough evaluation of my work. In addition, I would like to thank Alex Greaney for convincing me to enter the field of materials science, as well as my co-workers, both past and present, whom I have had the good fortune to know. This includes, but is not limited to Shuo Chen, Carolyn Sawyer, Matt Sherburne, Yuzhi Zhou, Tomohito Tsuru, James Mastandrea, Max Poschmann, and Maarten de Jong. Last of all, I would like to thank my family, in particular my parents and brother, for their love and unwavering support of my academic interests.

Chapter 1

Introduction

The continued increase in computational capabilities coupled with advancements in first-principles methods for calculating materials properties makes computational materials design a powerful tool in the development of materials. The computer-aided design of structural materials, however, lags behind that of other fields. This is due to the complexity of defect-mediated plasticity, which is known to be the predominant deformation mechanism in most metals [1, 2, 3]. Modeling defect-mediated plasticity from first-principles is especially difficult due to the different length and time scales involved in dislocation motion. For instance, a heavily cold-worked metal possesses a dislocation density on the order of $10^{11} - 10^{12}$ cm^{-2}, which would require approximately 100,000 atoms to simulate a straight dislocation dipole, while density functional theory (DFT) calculations are generally only feasible for systems with less than 1000 atoms. In addition, the mechanical behavior of a material is generally sensitive to factors such as temperature and strain rate, which either greatly increase the computational cost (temperature) or are impossible to match with first-principles methods (strain rate).

A good deal of progress has been made in computer-aided structural materials design, mostly in the form of multiscale modeling and the integrated computational materials engineering (ICME). Examples of successes in this field include the virtual aluminum casting program at Ford Motor Company [4] and the QuesTek's development of a corrosion-resistant landing-gear steel [5]. In both of these cases first-principles calculations were one part of an array of different models used in the design of the material with still a large degree of empiricism involved in the process. While these represent advances in computer-aided design they are geared towards optimizing the performance of conventional structural materials for which there is already a wealth of imformation. The development of gum metal in the early 2000s offers a possible path towards structural materials discovery based on first-principles calculations.

In 2003, gum metal, a class of Ti-Nb based alloys was developed by Toyota [6]. These alloys display numerous interesting properties, many of which only occur after the metal has been severely plastically deformed; this often means cold-swaging the material to more than a 90% reduction in area. As shown in Figure 1.1 gum metal possesses a yield strength of approximately 1.2 GPa, reasonable ductility (13% elongation to fracture), along with a high elastic limit (2.5%), and the absence of work hardening. Gum Metal's Young's modulus and thermal expansion coefficient are temperature insensitive over a wide temperature range. In addition, the thermal expansion coefficient is near zero over this same temperature range.

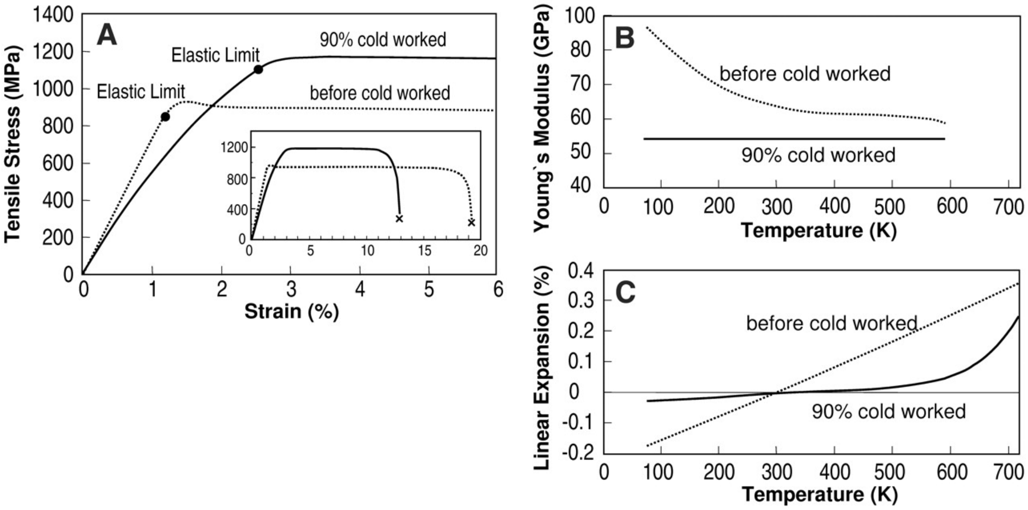

Figure 1.1: *Depiction of the mechanical and thermal properties of gum metal. From Saito et al. [6]. Reprinted with permission from AAAS.*

Gum Metal has the interesting combination of a low elastic modulus and a yield strength on the order of the ideal strength of the material. This observation initially lead to speculation that it could be the case of a material in which the ideal strength plays some role in the actual yield of the material. While this combination of properties may seem somewhat contradictory, lattice softening appears to be central to the behavior of gum metal. It was initially discovered by pushing a body-centered-cubic (BCC) Ti alloy towards the hexagonal close-packed (HCP) transition composition, which leads to a softening of the elastic constants [7]. Theoretical work by Li *et al.* showed that lattice softening can result in an increase in the susceptiblity of dislocations to pinning [8], allowing for mechanisms other than the dislocation motion to initiate plastic deformation. It was further asserted that two criteria must be met for a material to behave in a gum-metal-like fashion: 1) the material must be near an elastic instability in order to arrest dislocation motion and 2) it must be intrinsically ductile.

From a computer-aided design perspective these two criteria are especially attractive. The reason being that the elastic constants and ideal strength are some of the few mechanical properties of a material, that can be calculated accurately from first-principles [9, 10]. Further, ideal strength calculations can be used to assess a material's ductility [11]. The implication of this is that materials can be screened for their potential to act as a gum metal using first-principles calculations.

This dissertation presents the work that has gone into achieving this goal of evaluating potential gum-metal-like alloys. The first two chapters detail the potential for magnesium and lithium-magnesium alloys to display gum-metal-like behavior. Chapter 2 describes the behavior of BCC magnesium as a function of pressure in terms of its elastic properties. Chapter 3 uses the same approach as the first, but instead focuses on effects of composition in a lithium-magnesium alloy on the elastic properties and dislocation core. Chapter 4 outlines a general approach for searching for materials in which dislocations can be easily pinned. The final two chapters deal with the evaluation of a material's ductility. In chapter 5 a method is introduced for approximating the intrinsic ductility and ideal strength of a random solid solution. Chapter 6 demonstrates how this method can be generalized to produce an ideal yield surface. Finally, concluding remarks on this project are presented, including future work that can be done and the possible implications on this work in the field of structural materials design.

Chapter 2

Dislocations near elastic instability in high pressure body-centered cubic magnesium

Over a decade ago researchers at Toyota developed Gum Metal, a class of TiNb based metals that exhibit a wide variety of both novel and attractive properties [6]. These metals display an elastic limit of approximately $2 - 3\%$ at room temperature and 4% at 77 K, a yield strength of over 1 GPa, as well as Invar and Elinvar properties. In addition Gum Metal appears to fail at or near its ideal strength, a behavior that has been long thought impossible in a bulk material due to the prevalence of defect mediated plasticity [1, 2, 3]. Saito, *et al.* proposed three criteria for the emergence of the "super" properties of Gum Metal [6]. The material must have an average valence electron number (electron/atom ratio) of 4.24, a bond order of approximately 2.87 and a d-electron orbital energy level of roughly 2.45 eV.

Subsequent work on Gum Metal suggested that a more general connection can be made between the properties of Gum Metal and the proximity of a material to an elastic instability [8, 12, 13, 7]. Gum Metals exist near the composition at which the body-centered cubic (BCC) phase becomes elastically unstable and transforms into the hexagonal close-packed (HCP) phase. The proximity to this lattice instability is apparent in the elastic constants. Specifically the shear modulus, $C' = \frac{1}{2}(C_{11} - C_{12})$, goes to zero at the transition [6, 8]. Based on continuum anisotropic linear elasticity theory (henceforth abbreviated as linear elasticity theory) an explanation for the apparent failure of Gum Metal near its ideal strength has been developed. As the elastic instability is approached the dislocations' core radii grow. For proper alloy compositions and sufficient dislocation densities (Gum Metal's "ideal" behavior emerges only after severe cold-working[6]) an applied stress can cause the spread dislocation cores to percolate, resulting in high shear stress regions, where plastic deformation via shear melting should be possible [12].

This explanation for the appearance of Gum Metal like properties suggest that it might be possible to observe similar behavior in other alloy systems and at other types of lattice instability [13]. In fact, experimentally the BCC to face-centered cubic (FCC) instability has been exploited to produce a Fe-Ni-Co-Ti alloy with Gum Metal like properties [14]. As in the case of Gum Metal, the properties of this alloy are likely strongly influenced by the d-states of the component atoms. Experimentally, the only known examples of Gum Metals are based upon transition metals.

This suggests an interesting avenue of exploration. Can one develop a Gum Metal alloy without the incorporation of transition metal elements? Such an alloy might be technologically interesting as it is likely to have a high specific strength. For example, a Mg based Gum Metal might be well suited for applications requiring a light weight structural alloy. In what follows, we consider the potential for a non-transition metal to display properties that have been linked to the ”super” properties of TiNb based Gum Metals. We consider in detail the case of Mg under high pressure.

The BCC phase is elastically unstable in magnesium at ambient pressure [15], but is predicted to be stabilized at high pressures [16]. This offers a useful model for examining the effect of an elastic instability on the dislocation core structure as pressure can be used to approach the instability. It is also a much simpler approach compared to varying the composition of a binary alloy to approach an elastic instability, as none of the complexities inherent to modeling a solid solution need to be considered.

We first calculate the relative stability of BCC Mg with respect to HCP as a function of pressure using density functional theory (DFT) and compare these results to those already in the literature. By determining the elastic constants for a range of pressures, we show that BCC Mg approaches an elastic instability associated with $C' \to 0$ and that this corresponds to a spreading of the dislocation core. Analysis of the dislocation core structure indicates that interactions between the spread cores take place. This leads, initially, to the formation of localized regions of shear (nanodisturbances) that are characteristic of Gum Metal [17], and ultimately results in the nucleation of the HCP phase. Unlike Gum Metal, BCC magnesium is predicted to be intrinsically brittle, despite being highly elastically anisotropic and having a G/B value typically associated with ductility.

2.1 Theory

The calculation of elastic constants was done by following the method described by Sin'ko in which pressure terms are incorporated into the elastic constants [18]. The approach begins with writing the strain of the homogeneous body as a symmetric second-rank tensor, which is a function of the strain magnitude, γ, and is of the form

$$\epsilon_{ij} = s_{ij}\gamma, \tag{2.1}$$

where s_{ij} is the form of the strain tensor. The elastic constants can then be written as a function of both volume at a given pressure V, and the Lagrangian strain $\boldsymbol{\eta}$

$$\tilde{C}_{ijkl} = \frac{1}{V}\frac{\partial^2 E(V,\eta)}{\partial\eta_{ij}\partial\eta_{kl}}, \tag{2.2a}$$

$$\eta_{ij} = \epsilon_{ij} + \frac{1}{2}\epsilon_{ik}\epsilon_{kj}. \tag{2.2b}$$

It should be noted that the Einstein summation convention is used. Taking the Taylor series expansion of the strain energy with respect to the strain magnitude results in

$$\sum_{\alpha,\beta}\xi_\alpha\xi_\beta\tilde{C}_{\alpha\beta}s_\alpha s_\beta = P(V)\sum_\alpha \xi_\alpha s_\alpha^2 + \frac{1}{V}\frac{\partial^2 E(V,\gamma)}{\partial\gamma^2}|_{\gamma=0}. \tag{2.3}$$

The above equation is written in Voigt notation with the indices ranging from 1 to 6 and $\xi_\alpha = 1$ if $\alpha \leq 3$ and $\xi_\alpha = 2$ if $\alpha > 3$. Tsuchiya and Kawamura found that by selecting the strain configurations appropriately, the cubic elastic constants under pressure ($\tilde{C}_{ij}$) can be calculated from equation 2.3 using the following equations [19]

$$\tilde{C}_{11} = \frac{1}{V}\frac{\partial^2 E(V,\hat{\boldsymbol{\epsilon}}_4)}{\partial\gamma^2}|_{\gamma=0}, \tag{2.4}$$

$$\tilde{C}_{44} = -\frac{P}{2} + \frac{1}{12V}\frac{\partial^2 E(V,\hat{\boldsymbol{\epsilon}}_5)}{\partial\gamma^2}|_{\gamma=0}, \tag{2.5}$$

$$\tilde{C}_{11} - \tilde{C}_{12} = -P + \frac{1}{2V}\frac{\partial^2 E(V,\hat{\boldsymbol{\epsilon}}_6)}{\partial\gamma^2}|_{\gamma=0}. \tag{2.6}$$

Here the strain tensors $\hat{\boldsymbol{\epsilon}}_4$, $\hat{\boldsymbol{\epsilon}}_5$, and $\hat{\boldsymbol{\epsilon}}_6$ are defined as follows

$$\hat{\boldsymbol{\epsilon}}_4 = \begin{pmatrix} \gamma & 0 & 0 \\ 0 & 0 & 0 \\ 0 & 0 & 0 \end{pmatrix}, \tag{2.7a}$$

$$\hat{\boldsymbol{\epsilon}}_5 = \begin{pmatrix} 0 & \gamma & \gamma \\ \gamma & 0 & \gamma \\ \gamma & \gamma & 0 \end{pmatrix}, \tag{2.7b}$$

$$\hat{\boldsymbol{\epsilon}}_6 = \begin{pmatrix} \gamma & 0 & 0 \\ 0 & -\gamma & 0 \\ 0 & 0 & 0 \end{pmatrix}. \tag{2.7c}$$

For a tetragonal lattice the elastic constants at pressure can be calculated using the following six strains defined as $\hat{\boldsymbol{\epsilon}}_1^{tetr}$, $\hat{\boldsymbol{\epsilon}}_2^{tetr}$, $\hat{\boldsymbol{\epsilon}}_3^{tetr}$, $\hat{\boldsymbol{\epsilon}}_4^{tetr}$, $\hat{\boldsymbol{\epsilon}}_5^{tetr}$, and $\hat{\boldsymbol{\epsilon}}_6^{tetr}$, which are represented in tensor form as,

$$\hat{\boldsymbol{\epsilon}}_1^{tetr} = \begin{pmatrix} \gamma & 0 & 0 \\ 0 & 0 & 0 \\ 0 & 0 & 0 \end{pmatrix}, \tag{2.8a}$$

$$\hat{\boldsymbol{\epsilon}}_2^{tetr} = \begin{pmatrix} 0 & 0 & 0 \\ 0 & 0 & 0 \\ 0 & 0 & \gamma \end{pmatrix}, \tag{2.8b}$$

$$\hat{\boldsymbol{\epsilon}}_3^{tetr} = \begin{pmatrix} \gamma & 0 & 0 \\ 0 & \gamma & 0 \\ 0 & 0 & 0 \end{pmatrix}, \tag{2.8c}$$

$$\hat{\boldsymbol{\epsilon}}_4^{tetr} = \begin{pmatrix} \gamma & 0 & 0 \\ 0 & 0 & 0 \\ 0 & 0 & \gamma \end{pmatrix}, \tag{2.8d}$$

$$\hat{\boldsymbol{\epsilon}}_5^{tetr} = \begin{pmatrix} 0 & 0 & 0 \\ 0 & 0 & \gamma \\ 0 & \gamma & 0 \end{pmatrix}, \tag{2.8e}$$

$$\hat{\boldsymbol{\epsilon}}_6^{tetr} = \begin{pmatrix} 0 & \gamma & 0 \\ \gamma & 0 & 0 \\ 0 & 0 & 0 \end{pmatrix}. \tag{2.8f}$$

The applied strains states do not exactly correspond to the cubic case shown in equation 2.7. No difference was seen in the elastic constants of a cubic material when using equations 2.8 or 2.7. Applying these six strain states separately results in a system of equations involving the elastic constants. The resulting six elastic constants describing a BCT lattice are defined in equation 2.9 in terms of the pressure and the the second derivative of the energy with respect to γ as

$$\tilde{C}_{11}^{tetr} = \frac{1}{V}\frac{\partial^2 E(V, \hat{\boldsymbol{\epsilon}}_1^{tetr})}{\partial \gamma^2}|_{\gamma=0}, \tag{2.9a}$$

$$\tilde{C}_{12}^{tetr} = P - \frac{1}{V}\frac{\partial^2 E(V, \hat{\boldsymbol{\epsilon}}_1^{tetr})}{\partial \gamma^2}|_{\gamma=0} + \frac{1}{V}\frac{\partial^2 E(V, \hat{\boldsymbol{\epsilon}}_3^{tetr})}{\partial \gamma^2}|_{\gamma=0}, \tag{2.9b}$$

$$\tilde{C}_{13}^{tetr} = P - \frac{1}{2V}\frac{\partial^2 E(V, \hat{\boldsymbol{\epsilon}}_1^{tetr})}{\partial \gamma^2}|_{\gamma=0} - \frac{1}{2V}\frac{\partial^2 E(V, \hat{\boldsymbol{\epsilon}}_2^{tetr})}{\partial \gamma^2}|_{\gamma=0} + \frac{1}{2V}\frac{\partial^2 E(V, \hat{\boldsymbol{\epsilon}}_4^{tetr})}{\partial \gamma^2}|_{\gamma=0}, \tag{2.9c}$$

$$\tilde{C}_{33}^{tetr} = \frac{1}{V}\frac{\partial^2 E(V, \hat{\boldsymbol{\epsilon}}_2^{tetr})}{\partial \gamma^2}|_{\gamma=0}, \tag{2.9d}$$

$$\tilde{C}_{44}^{tetr} = -\frac{P}{2} + \frac{1}{V}\frac{\partial^2 E(V, \hat{\boldsymbol{\epsilon}}_5^{tetr})}{\partial \gamma^2}|_{\gamma=0}, \tag{2.9e}$$

$$\tilde{C}_{66}^{tetr} = -\frac{P}{2} + \frac{1}{V}\frac{\partial^2 E(V, \hat{\boldsymbol{\epsilon}}_6^{tetr})}{\partial \gamma^2}|_{\gamma=0}. \tag{2.9f}$$

Ideal tensile strength calculations can be performed to determine if a material is intrinsically brittle or ductile [20, 21]. The eigenvalues of the symmetrized Wallace tensor [22, 23], λ_{ijkl}, govern the elastic stability of a material following

$$\lambda_{ijkl}\delta\epsilon_{ij}\delta\epsilon_{kl} \geq 0. \tag{2.10}$$

In the case of a uniaxial load, σ, on a BCC material applied along $\langle 001 \rangle$ the elastic stability criteria are

$$(C_{33} + \sigma)(C_{11} + C_{22}) > 2\left(C_{13} - \frac{\sigma}{2}\right)^2, \tag{2.11a}$$

$$C_{11} - C_{22} > 0, \tag{2.11b}$$

$$C_{66} > 0, \tag{2.11c}$$

$$C_{44} + \frac{\sigma}{2} > 0. \tag{2.11d}$$

The failure of conditions 2.11b-2.11d correspond to a shear instability (intrinsic ductility) while condition 2.11a results in cleavage [24]. The elastic constants are of a body-centered tetragonal (BCT) Bravais lattice due to an uniaxial load being applied to the BCC crystal.

The elastic constants can be used to define a size for a dislocation core. By defining the dislocation core as the region for which the stress predicted by linear elasticity theory is greater than the ideal strength, an approximation for the region in which linear elasticity theory is no longer valid is obtained [12, 13]. Since symmetry often links the ideal strength to the elastic constants, this definition allows for the dislocation core radius to be written in terms of the elastic constants. In the case of a BCC metal the dislocation core radius can be expressed as

$$r_{core} = \frac{bK}{2\pi f G_{\langle 111\rangle}}. \tag{2.12}$$

Here b is the Burgers vector, K, the elastic modulus governing the dislocation line tension, $G_{\langle 111\rangle}$, the shear modulus along the $\langle 111\rangle$ direction (that for BCC is independent of slip plane), and, f, a constant equal to approximately 1/9 in the case of BCC [13]. K and $G_{\langle 111\rangle}$ can be expressed as

$$K = \sqrt{(C_{11}-C_{12})C_{44}}\sqrt{\frac{2C_{11}^2+2C_{11}C_{12}-4C_{12}^2+13C_{11}C_{44}-7C_{12}C_{44}+2C_{44}^2}{3(C_{11}-C_{12}+4C_{44})(C_{11}+C_{12}+2C_{44})}}, \tag{2.13}$$

$$G_{\langle 111\rangle} = \frac{3C_{44}(C_{11}-C_{12})}{C_{11}-C_{12}+4C_{44}}. \tag{2.14}$$

The result of equation 2.12 is that the dislocation core radius is inversely proportional to $\sqrt{C_{11}-C_{12}}$. It has been argued that in the case of Gum Metal, due to its small C' value the application of an applied stress can cause the dislocation core region to percolate resulting in paths of shear melting [12].

DFT can be used to compute dislocation core structures using periodic supercells of $\langle 111\rangle$ oriented screw dislocations following the approach of Daw [25]. This approach assumes that the distortion tensor can be written as a Fourier series

$$\Delta_{jk}(\mathbf{r}) = \sum_{\mathbf{G}} \tilde{\Delta}_{jk}(\mathbf{G})e^{i\mathbf{G}\cdot\mathbf{r}} \tag{2.15}$$

where $\tilde{\Delta}_{jk}(\mathbf{G})$ is a component of the distortion in reciprocal space and $\mathbf{G}$ corresponds to a reciprocal lattice vector. The elastic energy is written as

$$W_c = \frac{1}{2}C_{jklm}\int_{cell} dv\Delta_{jk}\Delta_{lm} = \frac{1}{2}\Omega_c C_{jklm}\sum_{\mathbf{G}}\tilde{\Delta}_{jk}\tilde{\Delta}^*_{lm}. \tag{2.16}$$

Here $\tilde{\Delta}^*_{lm}$ is the complex conjugate of $\tilde{\Delta}_{lm}$, C_{jklm} is the elastic tensor, and Ω_c is the volume of the cell. The equilibrium distortion tensor is determined by minimizing W_c with respect to the distortion components subject to the constraints imposed by the dislocations. The distortion is then integrated to produce the initial displacements for our unit cells. In our numerical work the core radius was chosen to be $b/4$. For a more in-depth discussion of this method see chapter 3.

The distortion in the cell vectors due to the introduction of the dislocation quadrupole was determined as done by Lehto and Öberg [26]. Analysis of the dislocation core structure was carried out using differential displacement maps (DD) as developed by Vitek *et al.* [27]. In these maps, the magnitude of an arrow between two nearest neighbor (NN) atoms shows the relative displacement, normal to the page, between the two atoms as a result of the dislocation. The arrows are scaled such that an arrow connecting NN represents a displacement of $b/3$. For a $\langle 111 \rangle$-type screw dislocation in BCC a full dislocation is symbolized in a DD map as a circuit which sums to b (e. g. a triangle of NN atoms connected by arrows of magnitude $b/3$ and pointing clockwise). The Nye tensor was calculated using the approach outlined by Hartley and Mishin [28, 29] .

2.2 Computational Details

The relative phase stability of BCC and HCP Mg, the elastic constants, dislocation core structure, and ideal tensile strength calculations were all performed using the projector augmented wave method (PAW) as implemented in the Vienna Ab Initio Simulation Package (VASP) [30, 31]. For the exchange-correlation functional the Perdew, Becke, and Ernzerhof (PBE) Generalized Gradient Approximation was employed [32]. Both the 2p as well as the 3s states were considered as valence electrons. Phase stability calculations using PAW were conducted using primitive unit cells. A plane-wave cutoff of 580 eV was used with a first-order Methfessel-Paxton scheme and a smearing parameter of 0.1 eV. The convergence conditions for energy and forces were set to 1×10^{-6} eV and 0.005 eV/Å respectively. These values were used for all other PAW calculations, unless otherwise stated. For BCC a $21 \times 21 \times 21$ Monkhorst-Pack grid was used, while for HCP a $21 \times 21 \times 13$ Γ-centered grid was implemented instead. The elastic constants calculations used a $25 \times 25 \times 25$ Monkhorst-Pack grid with a conventional BCC unit cell. Electronic relaxations for elastic constants calculations were set to 1×10^{-10} eV. A 135 atom BCC unit cell was used with $2 \times 1 \times 8$ Γ-centered grid for dislocation core calculations.

Ideal strength calculations [21, 20] were performed by applying a fixed strain along the [001] direction, as this is considered the weakest direction under tension for BCC metals [33, 34], and varying the strain along [100] and [010] to achieve the proper stress state. Relaxations were performed until all components of the stress tensor other than σ_{33} were less than 0.05 GPa. Brillouin zone integrations were performed using a $29 \times 29 \times 29$ Monkhorst-Pack grid. The intrinsic ductility of the material was tested by allowing the unit cell to relax along a tetragonal path. The symmetrized Wallace tensor was evaluated by calculating the BCT elastic constants using the same input parameters as for the cubic elastic constants described above. The strain states for the BCT elastic constants are defined in equation 2.8.

The relative phase stability as well as the density-of-states as a function of pressure were also performed using the full-potential linearized augmented plane wave (FP-LAPW) method as implemented in the code Elk [35]. Convergence testing was conducted with respect to the muffin-tin radius, k-point sampling, and plane-wave cutoffs. A total energy convergence criterion of 3.0×10^{-8} Ha was used.

2.3 Results

The phase stability of BCC and HCP structures was considered using both FP-LAPW and PAW. Both methods result in a general agreement for the behavior of the energy of the BCC phase in magnesium as a function of pressure as shown in Figure 2.1. This leads to the conclusion that the PAW method, while using the frozen-core approximation, models the given system reasonably well, and is suitable for our calculations. The BCC-HCP transition volume and pressure, computed with PAW, are in general agreement with previous work conducted using the linear muffin-tin orbitals method (LMTO) as shown in table 1. The current work's values for transition volume and pressure differ from that of reference [16] by 0.8% and 7% respectively. The partial density of states calculated using FP-LAPW shown in Figure 2.1d demonstrates that the occupation of the d-states are negligible at least for volumes $V = 0.6V_0$ and higher. Calculations of the density of states, Figure 2.2, at volumes between $0.6V_0$ and $0.7V_0$ using FP-LAPW show that the elastic instability does not appear to be related to the Fermi level approaching a van Hove singularity, which is associated with the low shear modulus, C_{44}, seen in V, Nb, and Ta [36, 37, 38]. Using the common tangent construction Figure 2.1 indicates that the two phase region does not extend far beyond the transition pressure, which is calculated to be approximately 50 GPa and corresponds to a volume of $0.6V_0$. However, the BCC phase remains elastically stable for volumes approaching V_0 as shown in Figure 2.3 and Table 2.2.

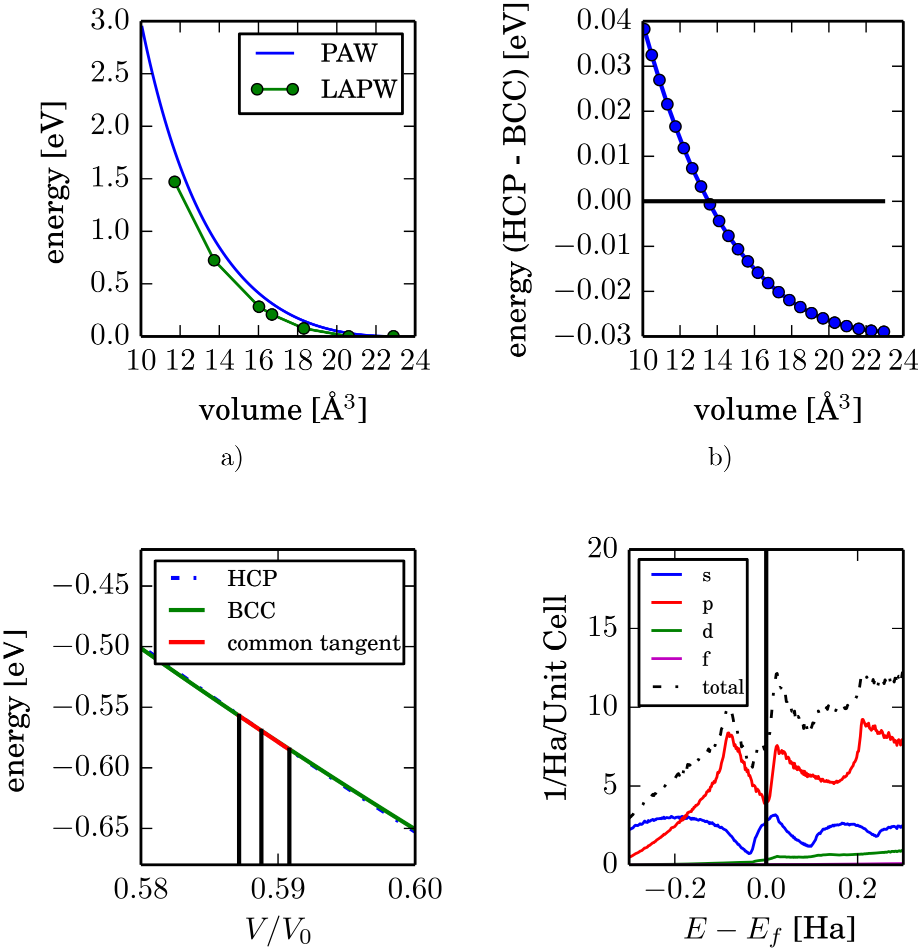

a) b) c) d)

Figure 2.1: *Comparison of the total energy of the BCC phase using both the FP-LAPW and PAW methods in 2.1a. Figure 2.1b shows a plot of the relative stability of BCC with respect to HCP as a function of volume. The BCC phase becomes stable at roughly half of the volume corresponding to ambient pressure and volume. Common tangent construction for BCC and HCP as a function of volume ratio is illustrated in Figure 2.1c. The partial density of states (DOS) for magnesium at* $V = 0.6V_0$ *is shown in figure 2.1d.*

The elastic stability of the BCC phase was computed and compared to previous work (Figure 2.3a). As ambient pressure is approached the BCC lattice becomes

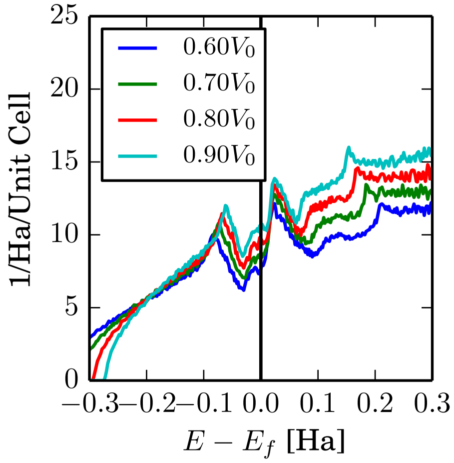

Figure 2.2: *Total density of states for volumes between* $0.60V_0$ *and* $0.90V_0$ *using FP-LAPW.*

Table 2.1: *BCC-HCP transformation data.* V_0 *corresponds to the volume of HCP magnesium under no applied pressure.*

V_0 (HCP) [Å^3]	V_{trans} [Å^3]	P_{trans} [GPa]	Ref.
23.0	13.5	53.8	current work
23.2	13	50	[16]
—	—	50 ± 6	[39]

elastically unstable. Based on the arguments given above this should result in an increase in the dislocation core radii. The dislocation core radius normalized by the burgers vector as calculated from elasticity theory is shown in Figure 2.3b. For volumes $0.6V_0 - 0.9V_0$ the core radius is large compared to Gum Metal, but also increases as the elastic instability is neared. For comparison the dislocation core radius of tungsten, a nearly elastically isotropic crystal, was estimated to be 1.45 b[12].

As shown in Table 2.2, the dislocation core radii of Gum Metal and the Ti_3Nb Gum Metal approximate are relatively close to the that of tungsten. The dislocation core radius of $Ti_{80}V_{20}$, however, is 2.42. Ti_3Nb contains 4.25 valence electrons per atom (e/a), while $Ti_{80}V_{20}$ has 4.20 e/a. Near an elastic instability small fluctuations

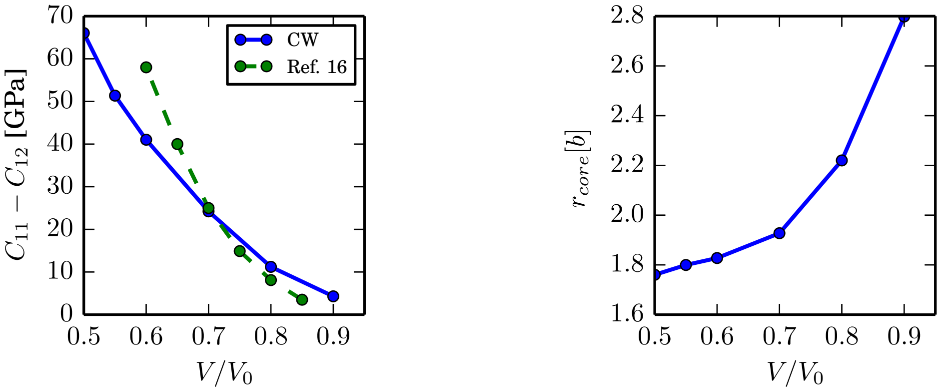

a) b)

Figure 2.3: *Figure 2.3a compares LMTO results from reference [15] with PAW (Current Work). Figure 2.3b shows the change in the ratio between the dislocation core radius, r_{core}, and magnitude of the Burgers vector, b. Lowering the pressure of Mg appears to cause $C_{11} - C_{12} \rightarrow 0$, leading the BCC phase to become elastically unstable.*

Table 2.2: *Comparison of relative core radii and elastic constants for various Gum Metal approximants. All elastic constants are in units of GPa.*

Material	C_{11}	C_{12}	C_{44}	C'	r_{core}/b
$Ti_{80}V_{20}$ (Theory) [12]	139	131	47	4	2.42
Ti_3Nb (Theory) [40]	149	111	37.5	18.7	1.51
Ti–36Nb–2Ta–3Zr–0.3O (wt.%) [41]	125	93	28	16	1.49
Mg ($V = 0.6V_0$)	207	178	124	14.5	1.83
Mg ($V = 0.7V_0$)	137	112	85.5	12.5	1.93
Mg ($V = 0.8V_0$)	84.2	76.1	59.9	4.05	2.51

in composition (changes in e/a) can have a dramatic impact on the dislocation core radius, leading to the potential for different mechanisms for plasticity in different regions of the material. Substituting pressure for composition this same behavior is apparent. Comparing figures 2.3a and 2.3b, as $C_{11} - C_{12}$ approaches zero the dislocation core radius increases.

Dislocations core structures were computed as described in section 2.2. A quadrupolar configuration for the dislocations was selected as this has been shown to be energetically favorable to a conventional dipole stacking [26]. Figure 2.4 illustrates the expansion of the dislocation cores in the quadrupolar configuration as the volume increases from 65% to 80% of the ambient volume coinciding with the drop in C' as seen in Figure 2.3. The dislocation densities of the screw quadrupolar configuration at $0.65V_0$, $0.70V_0$, and $0.80V_0$ is 2.66×10^{17} m^{-2}, 2.53×10^{17} m^{-2}, and 2.32×10^{17} m^{-2} respectively. It should be noted that the lateral displacements of atoms on the (111) plane are included in this plot. The large displacements shown in the DD map for the two larger volumes are indicative of the phase transformation of BCC to HCP as illustrated in Figure 2.4 by adaptive common neighbor analysis (a-CNA)[42] as implemented in the open visualization tool (OVITO) [43]. This is especially evident for $0.8V_0$, where the dislocations appear to have initiated the transformation of almost the entire supercell into HCP (red atoms). Considering that this material has been designed specifically such that C' approaches zero, the appearance of HCP in the dislocation core is understandable. The $0.65V_0$ dislocation cores display an approximant three-fold symmetry near the center of the dislocation similar to those found by Vitek, *et al.* for Fe [27]. These correspond to the three $\{112\}$ type planes intersecting the dislocation cores. Interestingly, the Burgers path, which connects the BCC to HCP phase [44] consists of a near $\{11\bar{2}\}\langle 111\rangle$ shear coupled with a softening of N-point acoustic phonon mode [45].

Figure 2.5 depicts the projection of a screw dislocation quadrupole with all atoms projected onto the (111) plane in order to better visualize any lateral shifts resulting from the dislocations. The large degree of lateral displacements for both volumes is associated with a highly anisotropic material based on a comparison to TiV dislocation cores [12]. In Figure 2.5a localized regions of shear can be seen reminiscent of nanodisturbances (defined as a dipole of partial dislocations with Burgers vectors not corresponding to the crystal) seen in Gum Metal [17] as well as TiV Gum Metal approximants [12]. In order to determine if the lateral displacements in the atoms claimed to be nanodisturbances in Figure 2.5 are associated with edge dislocations, the edge component of the Nye tensor was plotted for the dislocation quadrupolar configuration. From Figure 2.6 no edge character is apparent for either $0.65V_0$ or $0.7V_0$ BCC Mg. However, in the case of $0.8V_0$ there is a direct correspondence between the regions of possible edge character outlined in Figure 2.5 and the regions of high edge character in Figure 2.6, both of which are outlined by green circles in the two figures.

The pressure dependence of the ideal tensile strength was computed in order to explore the intrinsic brittle/ductile behavior of BCC magnesium. For the material to be intrinsically ductile it must fail under a uniaxial tensile load via a shear in-

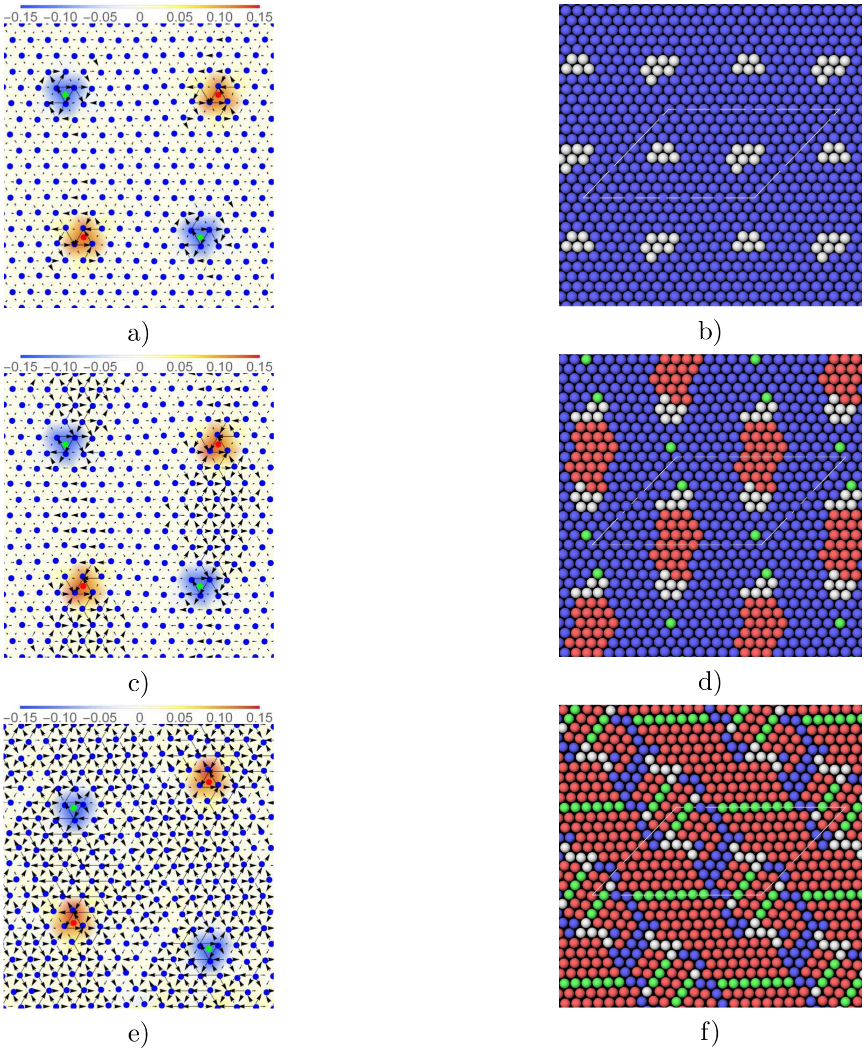

a) b) c) d) e) f)

Figure 2.4: *Comparison of relaxed* $\langle 111 \rangle$ *screw dislocations in a quadrupolar configuration for BCC magnesium at* $0.65V_0$, $0.7V_0$, *and* $0.8V_0$ *(figures a, c, and e respectively). Figures b, d, and f show atoms colored using CNA for* $0.65V_0$, $0.7V_0$, *and* $0.8V_0$. *Red atoms are HCP, blue atoms correspond to BCC, green FCC and white are unclassified.*

stability instead of via cleavage (intrinsically brittle). A failure of condition 2.11a is a consequence of a material being intrinsically brittle, as the eigenvector associated with this condition does not result in any shearing of the crystal. A uniaxial stress

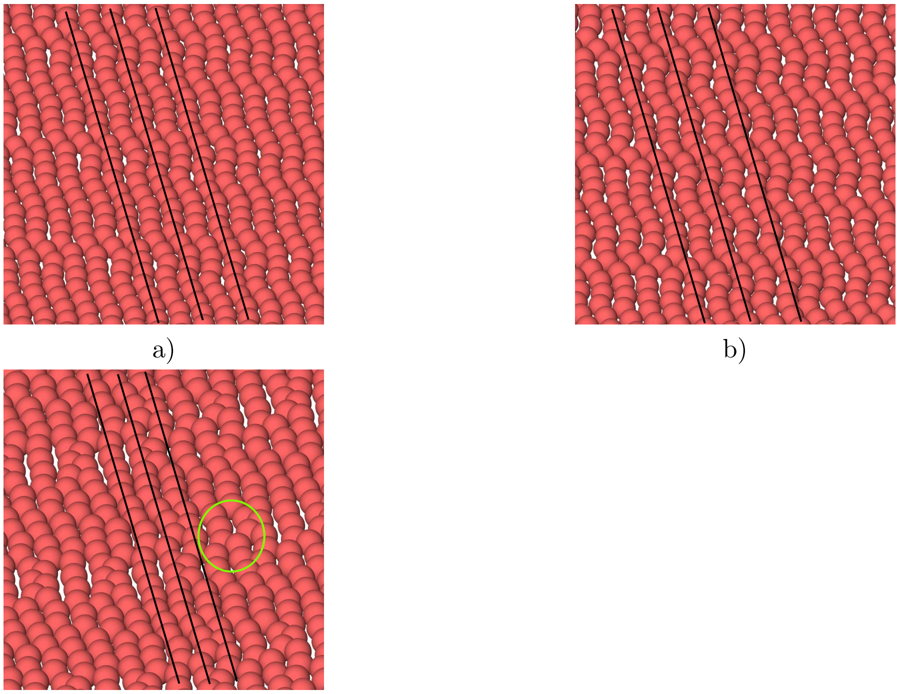

a) b) c)

Figure 2.5: *Projection of relaxed* $\langle 111 \rangle$ *screw dislocations in a quadrupolar configuration onto the* (111) *plane for BCC magnesium at* $0.65V_0$*,* $0.7V_0$*, and* $0.8V_0$ *(figures a, b, and c respectively). In Figure 2.5c, a region of suspected edge character is highlighted by the green circle.*

is applied along $\boldsymbol{c}$ and relaxations are performed under the constraint that the lattice remains BCT. The elastic stability at each strain is then determined from the eigenvalues of the symmetric Wallace tensor following equations 2.11a-2.11d.

BCC magnesium at both $0.65V_0$ and $0.7V_0$ is indicated to be intrinsically brittle as shown in Figure 3.4. Both volumes show an elastic instability due to cleavage at approximately $2\% - 4\%$ strain. The initial instability due to cleavage is relatively shallow, meaning that slight differences in the elastic constants could cause a change in behavior. This was tested by varying the smearing parameter. The elastic constants were run for smearings of 0.05 eV, 0.1, 0.2, and 0.3 eV. For all values the cause of elastic instability was found to be the same (cleavage).

The formation of an elastic instability at such small strains $2\% - 4\%$ is an unusual

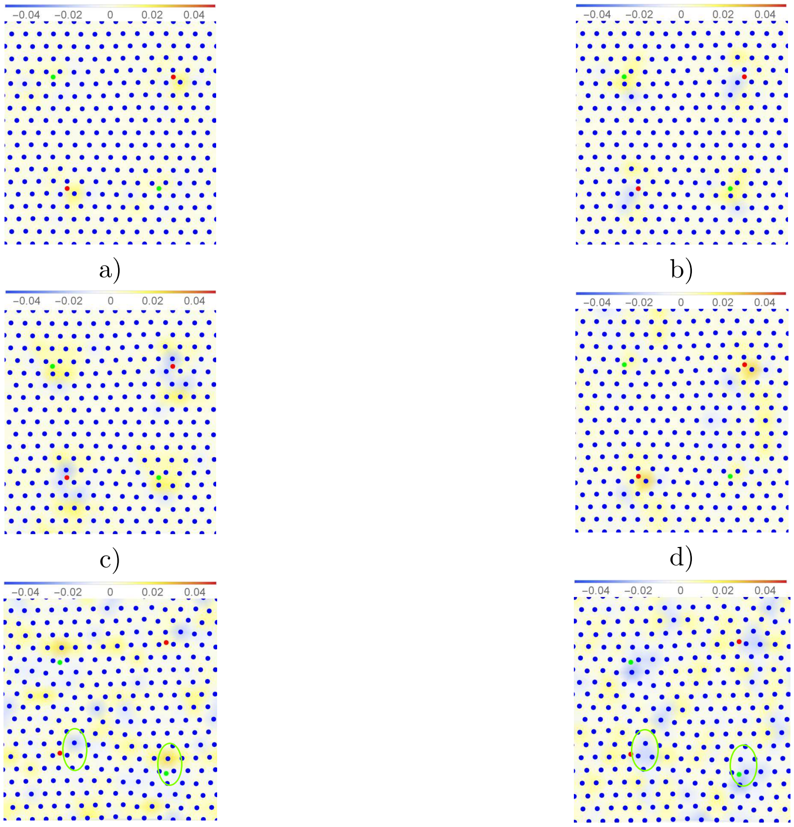

a) b) c) d) e) f)

Figure 2.6: *Comparison of relaxed* $\langle 111 \rangle$ *screw dislocations in a quadrupolar configuration for BCC magnesium at* $0.65V_0$, $0.7V_0$, *and* $0.8V_0$ *(first, second and third rows respectively). Coloring is done using the edge components,* α_{13} *and* α_{23}, *of the Nye tensor for the left and right columns respectively. The atom positions of plots show the lateral shifts resulting from the dislocations. The green circles identify regions that correspond to the regions of edge character in Figure 2.5.*

feature. Examining the change in the density of states as shown for the two volumes $0.65V_0$ and $0.70V_0$ in figures 2.8b and 2.8c, there does appear to be a large shift in the DOS for both volumes at the approximate energy range −2 eV to −1 eV. The application of an uniaxial load changes the point group of the crystal from O_h to D_{4h}. This causes the group of the wave vector along $Z_2 \to P$ to change from C_{3v} to C_{1h}. As C_{1h} has no 2 dimensional irreducible representation the band splits as shown in figure 2.8a. The same band splits at Z as a result of a change in the group of

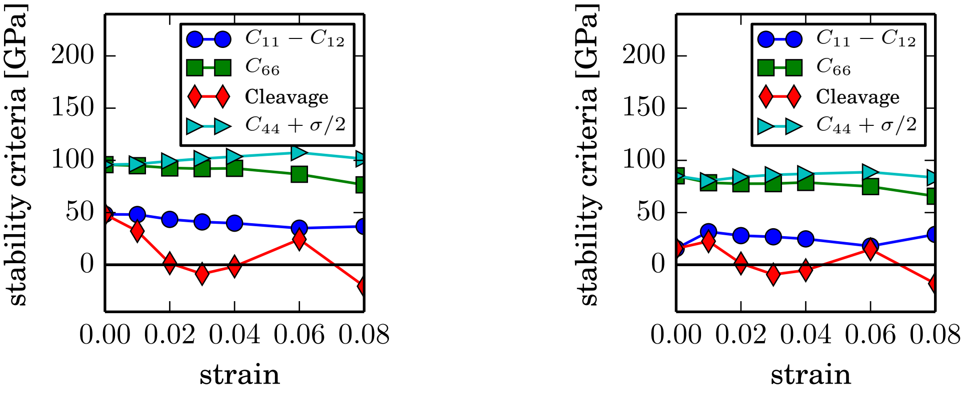

a) b)

Figure 2.7: *The eigenvalues of the symmetric Wallace tensor, which correspond to the elastic stability criteria of a crystal under an uniaxial load are shown for* $0.65V_0$ *and* $0.7V_0$ *in figures 2.7a and 2.7b respectively. Both volumes show an elastic instability at* $2\% - 4\%$ *that is a result of cleavage.*

the wave vector from O_h to D_{4h}. As shown in Figure 2.8a the splitting of this band appears to be associated with an overall increase in the energy of the occupied states ($Z_1 \rightarrow Z_2$). Interestingly, the two-fold degeneracy of the band at Z is consistent with that of a d-band [47]. There does appear to be some d-like character near and above the Fermi level as shown in Figure 2.1d, although it is much smaller than the s- and p-states. It does entertain the idea though that the d-electrons, while playing no significant role in bonding of the cubic crystal, could be involved enough in the strained state to contribute to the material failing in cleavage.

2.4 Discussion

BCC magnesium draws many parallels to Gum Metal. Linear elasticity theory shows that a reduction in C' with decreasing pressure is associated with an expansion in the dislocation core radius as well as an increase in the elastic anisotropy of the crystal. The strain field due to a screw dislocation contains more than one non-zero component for a highly anisotropic crystal leading to large lateral displacements. Dislocation core structure calculations show that as the pressure is reduced lateral displacements become more pronounced to the point where nanodisturbances appear. Associated with this is the formation of HCP via the Burgers path starting

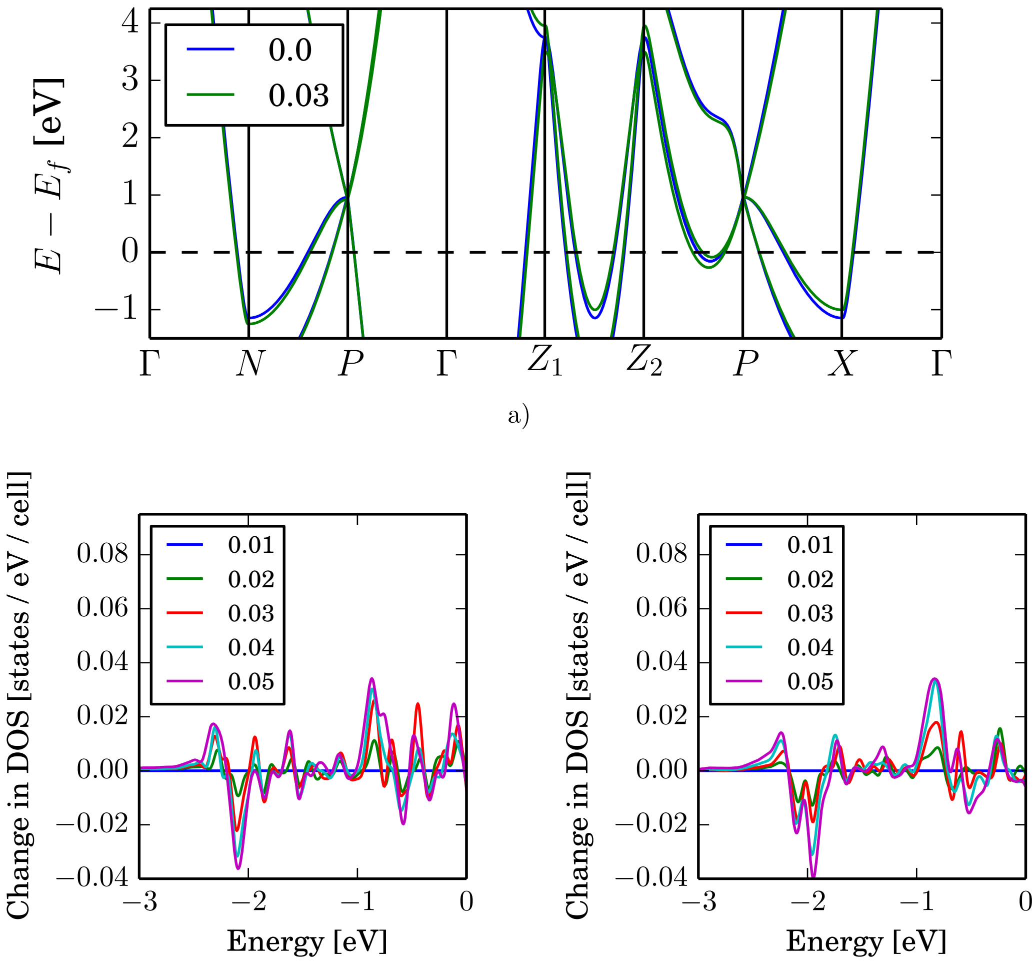

a)

b)

c)

Figure 2.8: *The band structure of* $0.65V_0$ *is shown with* 3% *applied strain and no strain (2.8a). The band structure of* $0.70V_0$ *resembles very closely that of* $0.65V_0$. *The change in the density of states with strain is shown in figures 2.8b and 2.8c. The high symmetry points are those of a body-centered tetragonal lattice [46]:* $\Gamma = [000]$, $N = \frac{1}{2}[100]$, $P = \frac{1}{4}[111]$, $Z_1 = \frac{1}{2}[11\bar{1}]$, $Z_2 = \frac{1}{2}[111]$, *and* $X = \frac{1}{2}[001]$. Z_1 *and* Z_2 *are symmetrically equivalent k-vectors in reciprocal space both corresponding to the high symmetry point, Z.*

at the dislocation core. These observations are all consistent with a previously stated explanation for ideal slip in a bulk material [12]. Heavily cold-working a material near an elastic instability results in a high density of dislocations, which exhibit large core structures. An applied stress can cause the dislocation core region to overlap, resulting in highly stressed regions in which shear bands associated with the Burgers path can form.

Unlike Gum Metal, BCC magnesium appears to be intrinsically brittle. With this noted, the behavior of BCC Mg is especially intriguing considering that the anisotropic Pugh ratio [48], $B/G_{\langle 111\rangle}$, for $0.7V_0$ BCC Mg is approximately 6.89, suggesting it is ductile. For comparison, values of the same ratio for niobium, vanadium, and tantalum (all intrinsically ductile BCC metals) are approximately 7.9, 5.5, and 3.3 respectively. As all calculations have been conducted at 0 K there is a possibility that a brittle to ductile transition can occur within the BCC phase.

Assuming that a material must (1) be near an elastic instability and (2) be intrinsically ductile for its plasticity to be governed by the ideal shear strength (ISS), the case for BCC magnesium appears to be in doubt. Condition (2) appears obvious for a perfectly crystalline material. However, bulk materials will always contain defects and if the theoretical studies on materials governed by ISS are to believed it is only at enormous defect densities that the ISS will begin to govern the yield strength. The complex stress fields associated with a high dislocation density bring into question whether a material must be intrinsically ductile to have its plasticity governed by the ISS.

2.5 Conclusion

The properties of BCC Mg nearing its elastic instability have been investigated using DFT. Calculations of the elastic constants at pressure show that C' of the BCC phase approaches zero with decreasing pressure, resulting in a highly anisotropic material for volumes $0.60V_0$ - $0.80V_0$. Dislocation core calculations show the formation of nanodisturbances between screw dislocations, which have been experimentally observed in Gum Metal. The formation of nanodisturbances is shown to coincide with the appearance of the HCP phase at or near the dislocation core. Ideal tensile strength calculations indicate that, unlike Gum Metal, BCC magnesium is intrinsically brittle. The lack of d-states in bonding for BCC magnesium leads to the suggestion that an intrinsically ductile material near an elastic instability could behave like Gum Metal.

Chapter 3

Behavior of Dislocations in BCC Lithium-magnesium Alloys

In the previous chapter, the connection between the presence of a crystal near a phase transormation and the emergence of gum-metal-like behavior was considered by examining the elastic constants and dislocation core spreading of BCC magnesium as a function of pressure. In this chapter the same idea of tuning a crystal to be near an elastic instability is considered, except in this case the system at hand is a lithium magnesium alloy and the method of tuning is the composition. In addition to the two gum metal indicators considered in the previous chapter (intrinsic ductility and a high value of K/G_{111}) the existence of ”soft” phonons along $\Gamma \rightarrow N$ is considered.

An investigation of the phonon dispersion can give further insight into a bulk material’s tendency to deform via a shear instability. The reduction in the reduced modulus and thus the decrease in ISS is associated with a softening of the acoustic phonons along $\Gamma \rightarrow N$ [45]. The softening of these phonons is also associated with the Burgers path [44] between the BCC and HCP phase. It has been shown that the softening of these phonons can result in shear faults similar to those seen in experiment [6].

Li-Mg alloys are suggested as an interesting candidate for Gum Metal like behavior for several reasons. The BCC phase is elastically unstable at ambient temperature and pressure in pure Mg [15]. In addition, the binary phase diagram shows no intermetallics and a large region of BCC stability [49]. Previous studies have demonstrated that after severe plastic deformation (SPD), either by equal-channel angular pressing[50, 51] (ECAP) or high pressure torsion[52] (HPT), on a two phase (BCC and HCP) 8 wt. % Li alloy superplasticity is achieved at a relatively low temperature. HPT was shown to induced superplasticity at 323 K ($0.37T_m$), with the strain rate sensitivity estimated to be 0.3, lower than 0.5, the value typically associated with plastic deformation via grain boundary sliding. This suggests that other mechanisms for plastic deformation could be present. Interestingly, the application of HPT on a Fe-Ni-Co-Ti alloy existing near a BCC to face-centered cubic (FCC) instability results in Gum Metal like properties, such as an elastic limit of approximately 2% and a yield strength of 2.3 GPa [14].

First principles investigations of a range of Li-Mg alloys have shown these alloys to have an especially low value of C' [53, 54]. Using the Pugh ratio (B/G) as a measure of ductility [48] ordered compounds of composition between 40 and 80 at. % Mg were shown to be brittle despite their low value for C'. However, Mn, Fe, Co, Ni, Cl and Cu were shown to increase the ductility of the ordered 50 at. % B2 structure [55] according to the Pugh Criterion.

In this chapter Li-Mg alloys are evaluated as Gum Metal candidates via the three aforementioned criteria: intrinsic ducility, high elastic anisotropy, and softening of the acoustic phonons along $\Gamma \rightarrow N$. Here, it is shown that the dislocation core radius and elastic anisotropy indicates that these alloys displays remarkable similarities to Gum Metal, including the apparent formation of nanodisturbances (nanoscale regions of local shear[17]) due to the interaction of core structures of $\langle 111 \rangle$ type screw dislocations. Further investigation of the ideal tensile strength of ordered structures of $LiMg_3$ finds the alloy to be intrinsically brittle. However, alloying options are identified to potentially engineer intrinsic ductility.

3.1 Dislocation Core

In the previous chapter it was shown that the screw dislocation core radius is inversely proportional to the square root of the two shear moduli, C_{44} and C', meaning that softening of either shear modulus would result in the expansion of the dislocation core. As a lattice instability is approached the dislocation core radius will expand. This makes binary Li-Mg especially interesting as its phase diagram shows only two stable phases (BCC and HCP) separated by a miscibility gap [49]. In addition the BCC phase is elastically unstable at ambient pressures suggesting that a lattice instability might be found as the concentration of magnesium is increased within a solid solution alloy.

The effect of composition on the dislocation core can be further analyzed with first principles calculation of dislocation core structures using periodic supercells of $\langle 111 \rangle$ oriented screw dislocations following the approach of Daw [25]. According to this approach the distortion tensor, defined as the gradient of the displacement field

($\Delta_{jk} = \frac{\partial u_j}{\partial x_k}$), can be written as a Fourier series

$$\Delta_{jk}(\boldsymbol{r}) = \sum_{\boldsymbol{G}} \tilde{\Delta}_{jk}(\boldsymbol{G}) e^{i\boldsymbol{G}\cdot\boldsymbol{r}}. \tag{3.1}$$

Where $\tilde{\Delta}_{jk}(\boldsymbol{G})$ is a component of the distortion in reciprocal space and $\boldsymbol{G}$ is a reciprocal lattice vector. This definition allows for the elastic energy to be written as

$$W_c = \frac{1}{2}\int_{cell} dv C_{jklm}\Delta_{jk}\Delta_{lm} = \frac{1}{2}\Omega_c C_{jklm}\sum_{\mathbf{G}} \tilde{\Delta}_{jk}\tilde{\Delta}^{*}_{lm}. \tag{3.2}$$

The initial form of a dislocation quadrupole configuration can then be obtained by minimizing the elastic energy defined by equation 3.2 with respect to the distortion tensor given the constraints imposed by the dislocations. The singularity of the dislocation is approximated as a Gaussian distribution with a smearing of $b/5$. The distortion in the cell vectors due to the introduction of the dislocation quadrupole is determined as done by Lehto and Öberg [26]. The distortion of the ith lattice vector can be written as follows

$$\Delta\mathbf{a}_i = \mathbf{a}_i + \mathbf{b}(\mathbf{a}_i \cdot \mathbf{n}_{cut})\frac{L_{cut}}{V_{cell}}, \tag{3.3}$$

where $\mathbf{n}_{cut}$ is a vector normal to the cut of the dislocation (in this case [010]), L_{cut} the distance between the two screw dislocations and V_{cell} the volume of the cell.

3.2 Phonon Behavior

Associated with the reduction in the value of C' is the softening of acoustic phonon modes. However, the computational cost of an accurate calculation of the phonon dispersion of a binary solid solution such as Li-Mg using density functional theory (DFT) is prohibitive. This is due in much part to the size of the unit cell needed to obtain a statistically representative distribution of atoms and the lack of any point symmetry in a random solution. A simplified phonon dispersion was calculated based off of the Born-von Kármán constants [56, 57]. In this case only nearest- and next-nearest-neighbor contributions to the dynamical matrix were included, resulting in four parameters (α_1, α_2, β_2, and γ_1) that can be determined from the elastic constants as well as the direct calculation of one phonon mode (in this case the H-phonon) [58].

$$2(\alpha_1 + \alpha_2) = a_0 C_{11}, \tag{3.4a}$$
$$2(\alpha_1 + \beta_2) = a_0 C_{44}, \tag{3.4b}$$
$$4\gamma_1 = a_0 (C_{12} + C_{44}), \tag{3.4c}$$
$$16\alpha_1 = M\omega_H^2, \tag{3.4d}$$

where a_0 is the lattice parameter and ω_H is the H-phonon frequency. The relation between the dynamical matrix and the Born-von Kármán for a given reciprocal vector, $\mathbf{q} = \frac{2\pi}{a_0}(p_1, p_2, p_3)$, can be defined as follows

$$\begin{aligned}\Phi_{11}(\mathbf{q}) = 8\alpha_1[1 - \cos(\pi p_1)\cos(\pi p_2)\cos(\pi p_3)] + 2\alpha_2[1 - \cos(2\pi p_1)] + ...\\ 2\beta_2[2 - \cos(2\pi p_2) - \cos(2\pi p_3)],\end{aligned} \tag{3.5a}$$
$$\begin{aligned}\Phi_{22}(\mathbf{q}) = 8\alpha_1[1 - \cos(\pi p_2)\cos(\pi p_3)\cos(\pi p_1)] + 2\alpha_2[1 - \cos(2\pi p_2)] + ...\\ 2\beta_2[2 - \cos(2\pi p_3) - \cos(2\pi p_1)],\end{aligned} \tag{3.5b}$$
$$\begin{aligned}\Phi_{33}(\mathbf{q}) = 8\alpha_1[1 - \cos(\pi p_3)\cos(\pi p_1)\cos(\pi p_2)] + 2\alpha_2[1 - \cos(2\pi p_3)] + ...\\ 2\beta_2[2 - \cos(2\pi p_1) - \cos(2\pi p_2)],\end{aligned} \tag{3.5c}$$
$$\Phi_{12}(\mathbf{q}) = 8\gamma_1 \sin(\pi p_1)\sin(\pi p_2)\sin(\pi p_3), \tag{3.5d}$$
$$\Phi_{23}(\mathbf{q}) = 8\gamma_1 \sin(\pi p_2)\sin(\pi p_3)\sin(\pi p_1), \tag{3.5e}$$
$$\Phi_{13}(\mathbf{q}) = 8\gamma_1 \sin(\pi p_3)\sin(\pi p_1)\sin(\pi p_2). \tag{3.5f}$$

The H-phonon frequency was calculated following the approach outlined by Ho, *et al.* [59]. The frequency was achieved by determining the curvature of the energy curve according to equation 3.6 where $U_\mathbf{q}$ is the amplitude of the wave, $\Delta E_\mathbf{q}$ the change in energy per atom as a result of the phonon, and M is the average atomic mass of the system

$$\Delta E_\mathbf{q} = \frac{1}{2} M \omega_\mathbf{q}^2 U_\mathbf{q}^2. \tag{3.6}$$

From the phonon dispersion not only can the dynamical stability of the material be determined, but the behavior of the $\Gamma \to N$ phonons can be considered. In BCC the N point corresponds to the $\langle \frac{1}{2}\frac{1}{2}0 \rangle$ direction in reciprocal space [60]. The softening of these phonons [45] is associated with the transformation from BCC to HCP via the Burgers path [44] and is an indication of proximity to the BCC/HCP transition.

3.3 Computational Details

The elastic constants, dislocation core structure relaxation, and phonon calculations were performed within the projector augmented wave method (PAW) as coded in the Vienna Ab Initio Simulation Package (VASP) [30, 31]. The Perdew, Becke, and Ernzerhof (PBE) Generalized Gradient Approximation exchange-correlation functional was employed [32]. The Li valence states were chosen to be 1s2s2p while for Mg the 2p and 3s states were considered to be the valence states. Unless otherwise noted a plane-wave cutoff of 400 eV was used with a first order Methfessel-Paxton scheme employing a smearing parameter of 0.1 eV. Ionic relaxations were performed until such that all forces were less than 0.005 meV/Å.

The elastic constants were caculated from a 16-atom special quasirandom structure (SQS) generated using the alloy theoretic automated toolkit (ATAT) [61]. Both pairs and triplet clusters were considered within a range of $3a_0$. Convergence tests were completed with respect to the number of K-points and varied depending on composition. However values were within the range of 1400 - 2000 points. As the SQS cell is not necessarily cubic the elastic tensor was symmetrized following the method of Tasnádi, *et al* [62]. The elastic constants were calculated performing 4 deformations of varying magnitude for the six independent strains and after obtaining the stresses from VASP via the Hellmann-Feynmann theorem performing a linear fit [63].

Ideal tensile strength calculations were performed by applying a strain along [001] and relaxing the other lattice vectors such that all stresses, using the Hellman-Feynmann theorem, apart from σ_{33} were below 0.05 GPa. The elastic constants at each strain were then determined using determined using a $21 \times 21 \times 21$ Monkhorst Pack grid.

For dislocation core structure calculations an initial cell consisting of 135 atoms was generated from elasticity theory. A 270 atom unit cell was then created by translating the unit cell by one lattice vector along [111]. The initial 270 atoms were then shuffled in order to create a disordered alloy at the desired composition. Atomic positions, but not the lattice vectors, were then relaxed using a $2 \times 1 \times 4$ Γ-centered grid. Analysis of the dislocation core structure was carried out using differential displacement maps as developed by Vitek, *et al.* [27]. Compositional effects on atom relaxations were corrected for by relaxing two cells of identical arrangement of atom types with one cell containing the dislocation quadrupole and the other being a perfect BCC lattice. Displacements in the perfect BCC random alloy were subtracted from displacements in the quadrupole configuration.

The H-phonon was calculated by generating 4 random configurations of a 16 atom unit cell of the desired composition. 4 configurations was deemed appropriate as all frequencies were within 2% of one another. The H-phonon was then applied to each cell with the amplitude of displacement ranging from -1% to 1% of the lattice parameter. Calculations were done using a $10 \times 10 \times 10$ Γ-centered K-point grid with a plane-wave cutoff energy of 500 eV.

3.4 Results

Figure 3.1 shows several noticeable trends in the ISS, elastic moduli, as well as core radius of of a $\langle 111 \rangle$ type screw dislocation. Li-Mg alloys appear to show a high ratio of the Young's modulus to shear modulus along $\langle 111 \rangle$, which is consistent with how Ti-V is found to behave [8]. As Figure 3.1c illustrates this behavior can be tied to the anisotropy parameter $K/G_{\langle 111 \rangle}$. The anisotropy parameter is also directly proportional to the dimensionless pinning length, l_c^* [8]. This parameter determines the average obstacle spacing necessary for a dislocation to be pinned.

The ISS estimated from the elastic constants appears to decrease with an increase in anisotropy. The ISS can be estimated as approximately 0.8 - 1.0 GPa at the BCC-HCP transition (approximately 75 at. % Mg). The resulting core radius predicted from elasticity theory is abnormally large. For reference the core radius of Tungsten is approximately $1.45b$ while that of Ti36Nb2Ta3Zr0.3O (wt.%) is $1.51b$ [64]. It is important to note that although the core radius of a $\langle 111 \rangle$ screw dislocation in Gum Metal does not appear to be that different than that of tungsten, because of the fact that Gum Metal exists near an elastic instability, composition fluctuations can lead to large dislocation core regions. This is illustrated in figures 3.1c, where the elastic anisotropy as well as the core radius increase rapidly near the elastic instability.

Dislocation Core Structure

DFT calculations of the dislocation core structure of a quadrupole configuration for $\langle 111 \rangle$ type screw dislocations as shown in Figure 3.2 shows a large degree of core spreading on the (111) plane in agreement with the results from elasticity theory. Of particular interest are the large lateral displacements of atomic columns shown in Figure 3.2b. The displacements become so large in areas that localized shearing of the crystal appears to have occurred. The structure is reminiscent of the nanodisturbances detected in Gum Metal [17]. The localized shearing occurs in the region between dislocation cores highlighted in Figure 3.2a. This same behavior has been identified in other investigations of Ti-V [12] and BCC Mg at high pressure [65]. It appears to suggest that the formation of these nanodisturbance like structures is a

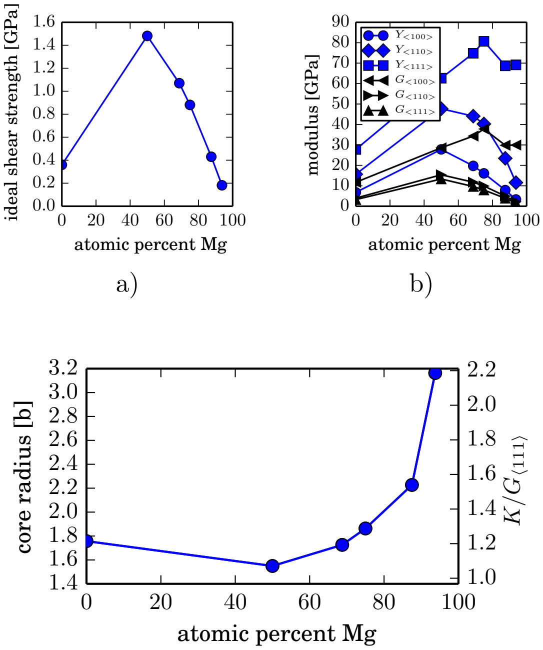

a)

b)

c)

Figure 3.1: *The ISS is estimated from the elastic constants of Li-Mg at various compositions (3.1a). A reduction in the ISS corresponds to a high degree of anisotropy between the Young's modulus and shear modulus along different axes (3.1b). A measure for the anisotropy of the crystal* $K/G_{\langle 111\rangle}$ *is shown to have a significant affect on the core radius (3.1c). The core radius at all compositions studied is higher than that predicted for Gum Metal.*

result of dislocation core interaction, possibly due to the overlap of spread dislocation cores.

Lattice Dynamics

All of the above observations regarding the formation of nanodisturbance like structures, spreading dislocation cores, as well as overall elastic anisotropy can be seen from the perspective of the approximated phonon dispersion. As the HCP phase is approached (Mg content is increased) Figure 3.3 shows the softening of the $\Gamma \rightarrow N$ branch. Specifically it can be shown that the lattice shuffling resulting from the N-phonon coupled with a near $\langle 1\bar{1}2\rangle\{111\}$ (approximately 13° from $\langle 1\bar{1}2\rangle$

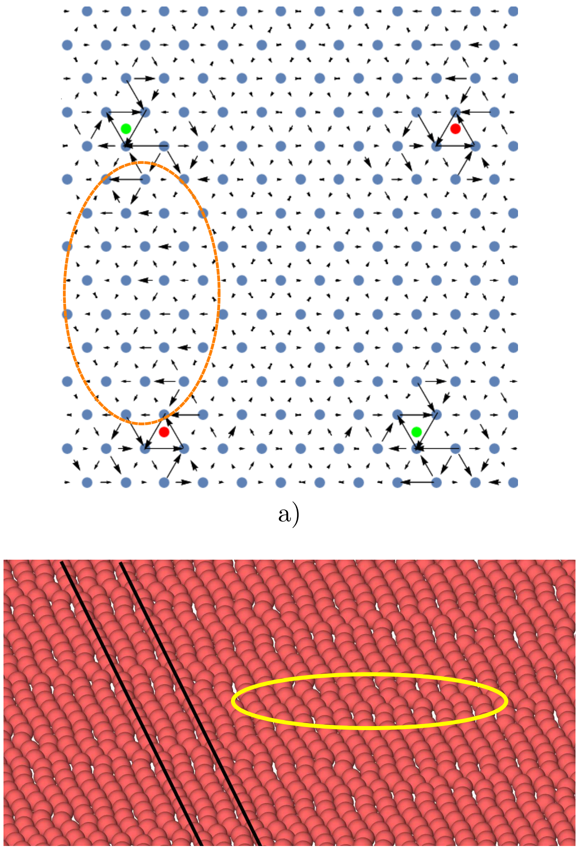

a)

b)

Figure 3.2: *The dislocation core (3.2a) shows a large degree of spreading. Along the vertical axis the region between dislocations appears to show large displacements (orange oval). The projection of atomic columns of onto the (111) is shown in 3.2b. Large lateral displacements are seen in the projection. For reference two straight black lines are drawn. Lateral shifts are especially large in the area within the yellow oval, which corresponds to the orange oval in 3.2a.*

on a {111} plane) transforms the BCC phase to HCP [45]. The orientation of the shear associated with this transformation is approximately the same as the large shear faults that have been reported in Gum Metal[6](13°). In addition, the N-phonon appears lower than the phonon associated with the transformation of BCC to the hexagonal ω phase [58], which corresponds to the lowest frequency between the P and H points in the dispersion ($\mathbf{q}_\omega \approx (\frac{1}{3}, \frac{1}{3}, \frac{2}{3})$). It seems then unlikely from these observations that a transformation path other than the Burgers path would be

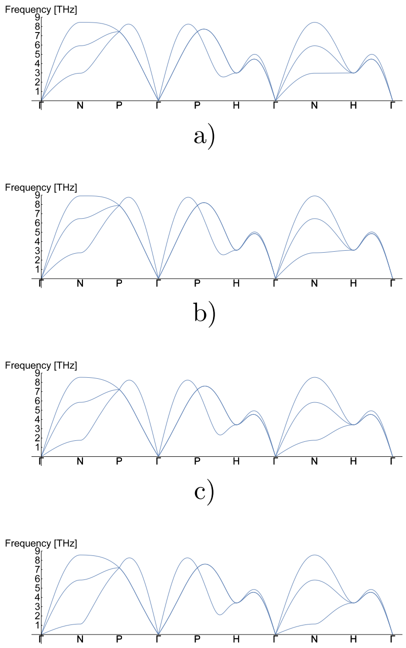

a)

b)

c)

d)

Figure 3.3: *The phonon dispersion is plotted for increasing compositions of Mg from 68.75 at. % (3.3a) 75 at. % (3.3b) 87.5 at. % (3.3c) and 93.75 at. % (3.3d). The formation of soft phonons along* $\Gamma \rightarrow N$ *can clearly be seen with increasing magnesium content.*

preferred.

Ideal Tensile Behavior

As described earlier, for a material to be a possible candidate for Gum Metal it must be intrinsically ductile. Ideal tensile strength calculations were carried out on two BCC-type ordered structures near the BCC-HCP transition (DO_3 and $L6_0$) to approximate the behavior of a Li-Mg alloy. These two structures were used to approximate a random alloy at this composition range. The DO_3 structure can be defined in terms of a primitive unit cell of the face-centered cubic lattice with four atoms of the form

$$\boldsymbol{a} = \frac{a_0}{2}(\mathbf{e}_2 + \mathbf{e}_3), \tag{3.7a}$$

$$\boldsymbol{b} = \frac{a_0}{2}(\mathbf{e}_1 + \mathbf{e}_3), \tag{3.7b}$$

$$\boldsymbol{c} = \frac{a_0}{2}(\mathbf{e}_1 + \mathbf{e}_2), \tag{3.7c}$$

$$\boldsymbol{\tau}_1 = \mathbf{0}, \tag{3.7d}$$

$$\boldsymbol{\tau}_2 = \frac{1}{4}\mathbf{a} + \frac{1}{4}\mathbf{b} + \frac{1}{4}\mathbf{c}, \tag{3.7e}$$

$$\boldsymbol{\tau}_3 = \frac{1}{2}\mathbf{a} + \frac{1}{2}\mathbf{b} + \frac{1}{2}\mathbf{c}, \tag{3.7f}$$

$$\boldsymbol{\tau}_4 = \frac{3}{4}\mathbf{a} + \frac{3}{4}\mathbf{b} + \frac{3}{4}\mathbf{c}. \tag{3.7g}$$

$L6_0$ is related to the $L1_2$ structure as BCC is related to FCC along the Bain path. According to Figure 3.4 the DO_3 structure displays cleavage failure at approximately 9% percent strain. This is in keeping with the behavior of the energy-strain curves for the tetragonal path of the two different structures, which show the stabilization of FCC at approximately $25 - 30\%$ strain. The material is preferentially following the Bain transformation path. Since FCC is shown from the energy curve to be metastable, a maximum stress must exist between the FCC and BCC phases, meaning that the material fails via cleavage; it is intrinsically brittle. This is in agreement with the estimate of the Pugh criterion [53].

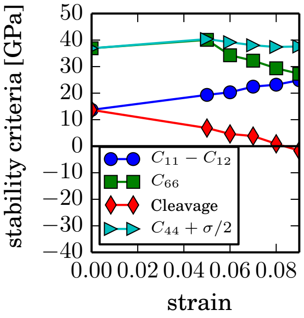

Figure 3.4: *The elastic stability criteria plotted as a function of strain for the DO_3 structure. The plot shows that a failure via cleavage is achieved at a strain of approximately* 9%.

a) b)

Figure 3.5: *The stress-strain and energy-strain relation for the DO_3 structure under a $\langle 100 \rangle$ type tensile load. Only the tetragonal path is explored in this simulation. The formation of the FCC phase can be seen at a strain of approximately* $25 - 30\%$

3.5 Discussion

From the first principles ideal tensile strength calculations it is not clear if the compositions of Li-Mg studied so far will behave as Gum Metal. This is due to the intrinsically brittle behavior seen for the ordered phases. Interestingly, Li, et al. found this to be the case for TiV alloys using the virtual crystal approximation [8] even at the special number of 4.24 valence electrons per atom. An initial guess at the origin of the brittle behavior comes from the plot of elastic moduli in Figure 3.1b where $\frac{G_{\langle 111 \rangle}}{Y_{\langle 100 \rangle}}$ is shown to be approximately 0.5. This is not only higher than the intrinsically ductile Nb and V whose values are approximately 0.15-0.25, but other intrinsically brittle BCC metals such as Mo and W with ratios of roughly 0.35 -

a)

b)

Figure 3.6: *The stress-strain and energy-strain relation for the* $L6_0$ *structure under a* $\langle 100 \rangle$ *type tensile load. Only the tetragonal path is explored in this simulation. The formation of the FCC phase can be seen at a strain of approximately* $25-30\%$. *This corresponds to the ordered* $L1_2$ *structure.*

0.40 [36]. However, this appears to only work for BCC materials that see an elastic instability as a result of $C_{66} \to 0$ for a [001] tensile load. Looking at the ratio of moduli in terms of the cubic elastic constants, which is written as

$$\frac{G_{\langle 111 \rangle}}{Y_{\langle 100 \rangle}} = \frac{3(C_{11}+C_{12})C_{44}}{(C_{11}+2C_{12})(C_{11}-C_{12}+4C_{44})} \tag{3.8}$$

shows that for $C_{11} = C_{12}$ the ratio becomes exactly $\frac{1}{2}$. While C' is soft, as Figure 3.4 shows, with the application of a uniaxial stress C' increases monotonically until failure occurs.

For the orthorhombic path to be activated in Li-Mg alloys (for intrinsic ductility to be obtained), the shear instability that initiates the orthorhombic path must be designed to occur before cleavage can occur. Within the face-centered orthorhombic (FCO) reference frame the condition $C_{11} - C_{12}$ must occur sooner in the tensile load. The tensile loading of a BCC crystal can result in two possible sequences of stress-free states. The BCC→FCC→BCT ordering is consistent with the tensile path while the BCC→BCT→FCC corresponds to an orthorhombic path [36, 66]. It follows that if the FCC phase could be made elastically unstable then the orthorhombic path would be preferred, and intrinsic ductility could be achieved. It is also possible that Li-Mg alloys undergo a brittle-ductile transition at some point below room temperature, which would negate the need to perform any alloying in order to achieve ductility. However, calculation of a brittle-ductile transition temperature from first-principles is an computationally challenging task.

If Li-Mg alloys can be tuned to be intrinsically ductile, then they become an intriguing structural material. Assuming that yield stresses near $40-50\%$ of the ISS could be reached, at a composition of 68.75 at. % Mg a specific strength of roughly 290-440 MPa $\text{cm}^3\ \text{g}^{-1}$ would be possible. In comparison Gum Metal is approximately 194 MPa $\text{cm}^3\ \text{g}^{-1}$ [6], while high-specific-strength steels (HSSS[67]) have been able to achieve specific strengths of approximately 190 MPa $\text{cm}^3\ \text{g}^{-1}$.

3.6 Conclusion

A first-principles investigation of the mechanical properties of a range of Li-Mg alloys is presented. Analysis of the elastic constants of solid solutions using special quasirandom structures shows many similarities in the behavior of the elastic constants of Li-Mg with those of Gum Metal as the BCC-HCP transition composition is approached. A large elastic anisotropy due to the softening of the reduced modulus results in a large nondimensional dislocation pinning length as well as large dislocation core radii. Associated with this is behavior is the emergence of large shear faults in the dislocation cores. As the material is found to be intrinsically brittle at all compositions studied more work is needed to make the structure intrinsically ductile.

Chapter 4

Computational Discovery of Gum-Metal-like Structural Alloys

The computational aided design of structural alloys is, by now, a well established field [68, 69, 5, 70]. Most often, computation is used to improve the properties of an existing structural material (e.g. steel, Ti, Al-alloys), and improvements are based on the fundamental understanding of the deformation mechanisms governing the mechanical properties of the alloys (e.g. dislocation slip vs. twinning). While the insights obtained are impressive and technologically important, they ultimately lead to improvements in relatively well-understood structural materials with well understood deformation mechanisms.

In contrast, the computational discovery of structural materials is far less common. Typically, the search has focused on identifying super-hard materials [71, 72, 73, 74, 75], as one can screen for these materials by evaluating combinations of the elastic constants. While super-hard materials will find structural applications, the broader class of structural alloys includes those that can be plastically deformed more extensively. To address this need, recent efforts focus on the discovery of high entropy alloys (HEAs) [76, 77]. Li et al. [78] note that dual phase HEA alloys can be made very strong *and* tough. The mechanisms invoked to explain this effect are the extreme solid solution strengthening observed in HEAs and a phase transformation induced hardening of the second phase. Notably, the improvement in mechanical properties is achieved by *reducing* the stability of the relevant phases.

In 2003, researchers at Toyota introduced a Ti-Nb based alloy that they named Gum Metal [6]. This body-centered-cubic (BCC) solid solution alloy displays numerous technologically interesting properties, many of which emerge only after extensive cold-working of the material. These properties include super-elasticity (an elastic limit of approximately 2.5% at room temperature), a near constant Young's modulus and zero thermal expansion coefficient from about 80 K - 550 K, little or no work-hardening while still displaying over 12% elongation, and a high yield strength (~1.2 GPa). Surprisingly, post mortem microstructural investigations revealed a dearth of dislocations [6]. This fact, when coupled with the observation that the strength of Gum Metal is comparable to its ideal shear strength (ISS), led Saito et al. to conclude that Gum Metal is a bulk engineering alloy that deforms at ideal strength.

This claim remains controversial as it seems to contradicts 80 years of metallurgical wisdom asserting that bulk alloys do not deform at ISS. Accordingly, the deformation of Gum Metal has attracted much attention, and the deformation mechanisms leading to its unusual behavior are beginning to be identified [8, 79, 80, 81, 82].

Since the early 1970's it has been known that TiNb alloys can display the shape memory affect [83]. Gum Metal was developed by tuning the composition of a TiNb alloy near instability by driving its shear modulus $C' = \frac{1}{2}(C_{11} - C_{12})$ to zero, placing the alloy near the β (BCC) to α (hexagonal-close-packed; HCP) transus [6, 84, 7]. The same approach has been applied to develop another Gum-Metal-like alloy that exploits proximity to the the face-centered-cubic (FCC) to BCC transition. This Fe-Ni-Co-Ti alloy is ductile (elongation to fracture of 9.4%) while having a yield strength of 2.2 GPa [14]. So known Gum Metals are similar to the tough, ductile HEAs [78] in that they, too, have been engineered to be near the limits of structural stability.

4.1 Theory

Theoretical work suggests that Gum-Metal-like behavior is possible near an FCC to HCP transition as well [13]. Moreover, the form of the elastic anisotropy that develops at the transitions between BCC, FCC and HCP phases can spread the dislocation cores [12, 13] and make the dislocations extremely susceptible to pinning by obstacles (and consequently extremely susceptible to solid solution strengthening), even at stresses approaching ISS [8]. Moreover, the spreading and overlap of dislocation cores can lead to the appearance of nanodisturbances in the microstructure [17, 12], a defect structure observed in Gum Metal. Interestingly, all of these properties can be deduced from a simple calculation of the elastic constants of the materials, and from computation of their ideal strengths [8, 12, 13, 21, 20, 36, 85]. So, while the deformation mechanism active in Gum Metal remains controversial, the materials properties that lead to Gum-Metal-like behavior can be identified.

This observation enables a purely computational four step approach to the discovery of Gum-Metal-like alloys: (1) Develop a general elastic anisotropy parameter, A_c, that is related to the susceptibility of a dislocation to being pinned and can be used to construct a structure map. (2) Evaluate this parameter for a set of materials. (3) Screen for materials of especially high anisotropy A_c. (4) Assess the elastic stability of solid solution alloys with the same composition.

Using the elastic constants in the Materials Project database [86, 87], we consider the cubic materials in space groups 225 and 229, and identify alloys with the propensity to display Gum-Metal-like behavior. Many of the identified alloys are known shape memory alloys. Of these, alloys based on the Al-Cu or Al-Cu-Mn system seem most promising technologically. Consequently, these are explored in more detail.

The means by which elastic anisotropy impacts dislocation core structures leads to a suitable definition of A_c. A requirement for a material to fail at its ideal strength is that the stress needed to initiate dislocation motion must be greater than ISS. This stress can be estimated using a simple two-dimensional line tension model that looks at the interaction of a dislocation with a random array of infinitesimal pinning sites [88]. The critical shear stress for dislocation motion in this model scales inversely with the average distance between pinning sites and scales linearly with the dislocation energy factor.

By equating the critical shear stress for dislocation motion to ISS, the critical non-dimensional average pinning length of obstacles, $l_c^* = l/b$ can be determined [8]. For many systems, it is reasonable to assume that ISS scales with a particular shear modulus, $G_{\{hkl\}\langle uvw\rangle}$. Taking as an example the case of a $\langle 111\rangle$ type screw dislocation in BCC, the ISS can be approximated as $\sigma_{ideal} = 0.11G_{\langle 111\rangle}$[24]. (Note that the shear modulus along $\langle 111\rangle$ is isotropic with respect to the shear plane for BCC.) The modulus governing the dislocation line tension can be determined analytically in terms of the elastic constants. This results in $l_c^* \propto \frac{K_s}{G_{111}}$, with

$$\frac{K_s}{G_{111}} = \sqrt{\frac{(C_{11} - C_{12} + 4C_{44})(2C_{11}^2 + 2C_{11}C_{12} - 4C_{12}^2 + 13C_{11}C_{44} - 7C_{12}C_{44} + 2C_{44}^2)}{27C_{44}(C_{11} - C_{12})(C_{11} + C_{12} + 2C_{44})}}. \tag{4.1}$$

The ratio $K_s/G_{\langle 111\rangle}$ can be viewed as an anisotropy parameter (in an isotropic material, the ratio is one). For the screw dislocations in BCC crystals, the ratio is inversely proportional to $\sqrt{C_{11} - C_{12}}$ and $\sqrt{C_{44}}$. As an elastic instability is approached and these shear moduli approach 0, $K_s/G_{\langle 111\rangle} \to \infty$, and l_c^* diverges. Similar behavior is found to accompany the elastic instability of edge dislocations in BCC [8] and for dislocations in materials near to other phase transitions [13]. Materials with large values of the anisotropy parameter $\frac{K}{G}$ have the potential to display Gum-Metal-like behavior.

An elastic anisotropy parameter for any crystalline system can be derived from Stroh's formalism [89]. Accordingly, the general non-dimensional elastic anisotropy parameter related to the pinning of dislocations is defined to be

$$A_c = \frac{b_p K_{pq} b_q}{b^2 G_{min}}, \tag{4.2}$$

where G_{min} is the smallest shear modulus oriented along the Burgers vector and $\boldsymbol{K}$ is the modulus associated with the energy factor of a dislocation, with Burgers vector $\boldsymbol{b}$.

The modulus of the energy factor ($\boldsymbol{K}$) of an arbitrary straight dislocation is derived from Stroh's formalism [89], which can be used to solve the elastic field of a straight dislocation in an anisotropic continuum. In these problems the displacement can be written in terms of position, $\boldsymbol{x}$, as

$$u_k(\boldsymbol{x}) = \sum_{\alpha=1}^{6} A_{k\alpha} D_\alpha f(\boldsymbol{m} \cdot \boldsymbol{x} + p_\alpha \boldsymbol{n} \cdot \boldsymbol{x}). \tag{4.3}$$

The orthonormal basis set consisting of $\boldsymbol{m}$, $\boldsymbol{n}$, and $\boldsymbol{t}$ forms the coordinate system, while p_α is a complex variable, D_α is a boundary condition dependent constant, and $A_{k\alpha}$ is a complex constant. In addition to $A_{k\alpha}$ it is useful to define an additional vector, $L_{k\alpha}$, which is defined in terms of $A_{k\alpha}$ and the elastic constants, C_{ijkm}, as

$$L_{j\alpha} = \frac{1}{p_\alpha}(mm)_{jk} A_{k\alpha} + (mn)_{jk} A_{k\alpha}, \tag{4.4}$$

with Einstein summation notation assumed. Here the parenthesis are used as a short hand notation: $(mm)_{jk} \equiv m_i C_{ijkr} m_r$. In the case of a dislocation with a line direction along $\boldsymbol{t}$ with no external forces present the displacement can be written as[90]

$$u_l(\boldsymbol{x}) = -\frac{1}{2\pi i} \sum_{\alpha=1}^{6} A_{l\alpha} L_{s\alpha} b_s \ln(m_q x_q + p_\alpha n_q x_q). \tag{4.5}$$

The stress field can then be represented as

$$\sigma_{jk} = -\frac{C_{jklr} b_s}{2\pi i} \sum_{\alpha=1}^{6} A_{l\alpha} L_{s\alpha} \frac{m_r + p_\alpha n_r}{m_q x_q + p_\alpha n_q x_q}. \tag{4.6}$$

The energy factor associated with the dislocation can be found by calculating the work done against the force generated from the creation of the dislocation [91]. This amounts to an energy per unit length of $\frac{W}{L} = \frac{1}{2} b_j \sigma_{jk} n_k$, allowing for the energy factor to be written in terms of $\boldsymbol{L}_\alpha$ and $\boldsymbol{A}_\alpha$ as

$$E = b_l \left(\frac{i}{4\pi} \sum_{\alpha=1}^{6} \pm L_{l\alpha} L_{s\alpha} \right) b_s. \tag{4.7}$$

In which the ± signifies a positive sign for $\alpha = 1, 2, 3$ and a negative sign for $\alpha = 4, 5, 6$. Noting that the definition of $\boldsymbol{K}$ is

$$K_{jk} = \frac{i}{4\pi} \sum_{\alpha=1}^{6} \pm L_{j\alpha} L_{k\alpha}, \tag{4.8}$$

the energy factor can be defined as $E = b_j K_{jk} b_k$.

The integral formalism[90] can be used to solve for $\boldsymbol{K}$ numerically. The integral formalism is based on the principle that the vectors $A_{k\alpha}$ and $L_{k\alpha}$ can be shown to be invariant to rotations of the basis vectors $\boldsymbol{m}$ and $\boldsymbol{n}$ about the $\boldsymbol{t}$ axis by an arbitrary angle, ω, and that p_α must obey

$$\int_0^{2\pi} p_\alpha d\omega = \pm 2\pi i. \tag{4.9}$$

With these main points in hand it can be shown that

$$K_{js} = \frac{i}{8\pi^2} \int_0^{2\pi} \left[(mm)_{js} - (mn)_{jr} (nn)^{-1}_{rk} (nm)_{ks} \right] d\omega. \tag{4.10}$$

A_c can be evaluated for hundreds of compounds in a matter of minutes. One can then construct an A_c-based structure map by plotting the points $\left(A_c^{screw}, A_c^{edge}\right)$ for each of the considered materials, with $A_c^{screw}(A_c^{edge})$ the computed anisotropy for screw(edge) dislocations with a given Burgers vector.

4.2 Results

To construct the structure map, A_c was computed for all materials in the Materials Project [86] elastic constants database with symmetry spacegroups $Im\bar{3}m$ (229) and $Fm\bar{3}m$ (225). Spacegroup 229 contains BCC while spacegroup 225 encompasses FCC as well as ordered structures with atomic positions consistent with BCC such as D0$_3$ and L2$_1$. Calculations of A_c were carried out for both screw and edge dislocations with Burgers vectors in the direction $\langle 111 \rangle$ and $\langle 110 \rangle$. In the case of edge dislocations the slip systems used were $\langle 111 \rangle \{1\bar{1}0\}$ and $\langle 110 \rangle \{1\bar{1}1\}$.

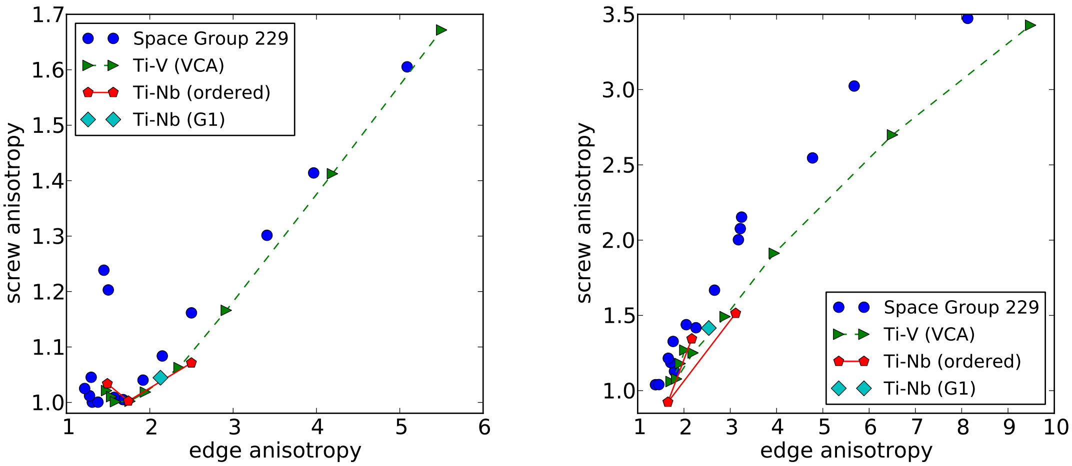

a) b)

Figure 4.1: *Comparison of the anisotropy parameter of the 15 materials with space group 229 with selected Ti-Nb and Ti-V systems for both an edge and screw dislocation for Burgers vectors oriented in the* $\langle 111 \rangle$ *(4.1a) and* $\langle 110 \rangle$ *(4.1b) directions. For the edge dislocations this corresponds to a* $\langle 111 \rangle \{110\}$ *slip system in Figure 4.1a and a* $\langle 110 \rangle \{111\}$ *slip system in Figure 4.1b. The Ti-Nb ordered systems consist of 25, 50, and 75 at. % Ti[7]. The VCA calculation consists of nine compositions at 5, 15, 25, 35, 45, 55, 65, 75, and 80 % Ti system[8, 12]. The G1 structure is known to be the lowest energy 16 atom configuration for 25 at. % Ti as calculated in DFT[40].*

Viewing the plots of the $\langle 111 \rangle$ and $\langle 110 \rangle$ type Burgers vectors for the $Im\bar{3}m$ (Figure 4.1) and $Fm\bar{3}m$ (Figure 4.2) space groups it can be seen that depending on the Burgers vector used A_c values change greatly. For instance the highest value of A_c^{screw} in Figure 4.1 is approximately 1.6 for $\boldsymbol{b} = \langle 111 \rangle$ and 3.5 for $\boldsymbol{b} = \langle 110 \rangle$. However, as the point of this plotting procedure is to identify outliers, the fact that the same ordering of materials by anisotropy is seen regardless of which Burgers vector is used in the calculation is an important finding. For instance, in the case of the space group 225 compounds the Spearman rank correlation coefficient between the two slip directions is 0.998 and 0.790 for a screw and edge dislocation respectively.

The structure maps reveal interesting trends. First, consider the Ti-Nb and Ti-V approximants to Gum Metal plotted in FIGs. 1 and 2. When viewed on

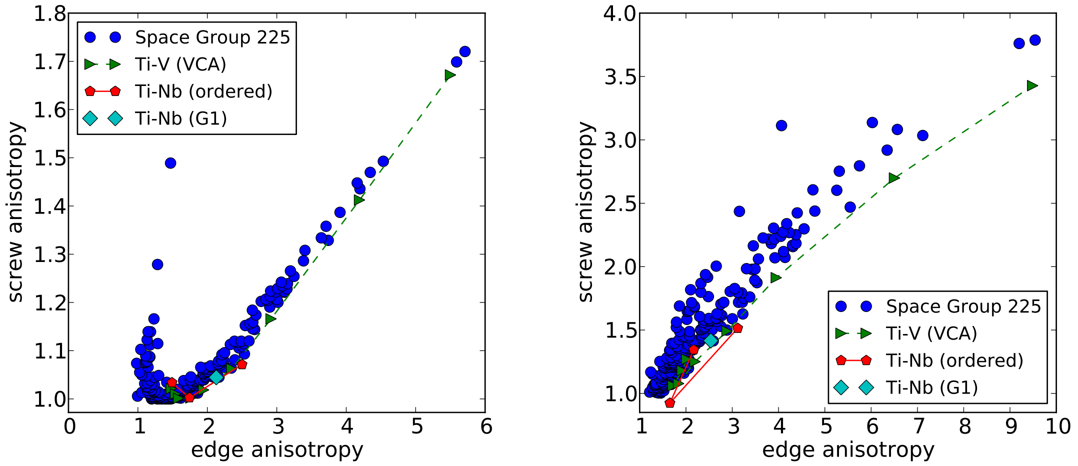

a) b)

Figure 4.2: *Comparison of the anisotropy parameter of the 227 materials with space group 225 with selected Ti-Nb and Ti-V systems for both an edge and screw dislocation for Burgers vectors oriented in the* $\langle 111\rangle$ *(4.1a) and* $\langle 110\rangle$ *(4.1b) directions. For the edge dislocations this corresponds to a* $\langle 111\rangle\{110\}$ *slip system in Figure 4.1a* and a $\langle 110\rangle\{111\}$ *slip system in Figure 4.1b. See 4.1 for more information on Ti-Nb and Ti-V systems.*

the structure map, the Ti-Nb approximants to Gum Metal do not have the most extreme A_c's of the compounds plotted. However, Gum Metal itself is a much more complicated alloy than the approximants and can include signficant additions of O, Hf, Ta, Zr and V. The Ti-V approxmants to Gum Metal, as computed using the virtual crystal approximation, reveal that the anisotropy ratios can be very sensitive to the number of valence electrons. Small changes in valence electron count can lead to large changes in A_c. Near the point of instability, a 10% change in valence electron count leads to almost a factor of two change in A_c^{edge}. So it is possible that while Ti-Nb does not itself possess an extreme A_c, the effects of alloying additions may lead to a substantially larger A_c than computed here. Importantly, the map reveals that there are stoichiometric intermetallic compounds that have larger A_c's than the prototypical alloy. These are the compounds of interest.

Figure 4.2 shows a noticeable branching in the data, especially at higher screw dislocation anisotropies, alluding to a certain dependence between the edge and screw dislocation anisotropies. It is difficult to discern the exact relation between the shown edge and screw dislocations as no simple analytic solution for the edge components of $\boldsymbol{K}$ exists for the given edge slip systems [91]. However, a simple solution exists for the $\langle 110\rangle\{001\}$ slip system and as Figure 4.3 shows, it gives results qualitatively in agreement with the$\langle 110\rangle\{1\bar{1}1\}$ system.

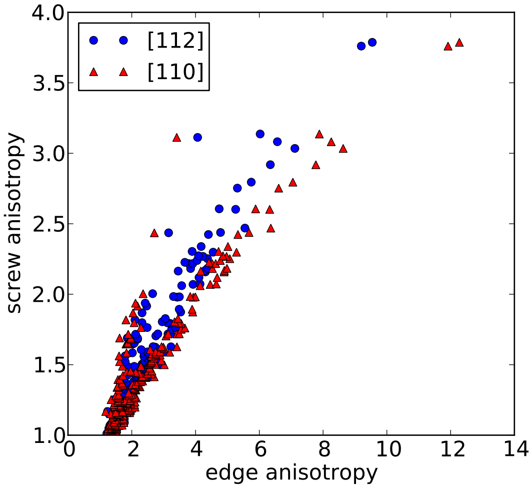

Figure 4.3: *Comparison of the analytically derived results for the* $\langle 110\rangle\{001\}$ *slip system (denoted* [110]*) with the numerically computed* $\langle 110\rangle\{1\bar{1}1\}$ *edge slip system (denoted* [112]*). Note that as the Burgers vector is the same for both calculations, the screw anisotropy is equal.*

For all slip directions and planes, a splitting behavior is seen at high anisotropy with the left branch appearing almost linear and the right branch trending sublinear with increasing edge anisotropy. Analysis of the $\langle 110\rangle\{001\}$ slip system suggests that the branches arise because of two different types of instability: $C_{44} \rightarrow 0$ and $C_{11} - C_{12} \rightarrow 0$.

For all structure maps presented in this work a splitting behavior is seen at high anisotropy with the left branch appearing almost linear and the right branch losing a linear dependence with increasing edge anisotropy. While numerical methods must be employed in order to evaluate $\boldsymbol{K}$ of a general straight dislocation, there are certain orientations in which a simple analytical solution of $\boldsymbol{K}$ does exist. In the $\langle 110\rangle\{001\}$ slip system $\boldsymbol{K}$ has two edge components (K_{e_y} and K_{e_x}) and a screw component (K_s) expressed in terms of the elastic constants as[91]

$$K_{e_x} = \frac{C_{11} + 3C_{12} + 2C_{44}}{2}\sqrt{\frac{C_{44}(C_{11} - C_{12} + 2C_{44})}{C_{11}(C_{11} + 3C_{12} + 6C_{44})}}, \tag{4.11a}$$

$$K_{e_y} = (C_{11} + 3C_{12} + 2C_{44})\sqrt{\frac{C_{44}(C_{11} - C_{12} + 2C_{44})}{2(C_{11} + C_{12} + 2C_{44})(C_{11} + 3C_{12} + 6C_{44})}}, \tag{4.11b}$$

$$K_{ss} = \sqrt{\frac{(C_{11} - C_{12})C_{44}}{2}}. \tag{4.11c}$$

By utilizing the above equations the slope of the data can be approximated as K_{ss}/K_{e_x}. As high anisotropy is generally a result of either $C_{44} \to 0$ or $C_{11} \to C_{12}$ it is of interest to explore K_{ss}/K_{e_x} and K_{ss}/K_{e_y} in these limits:

$$\lim_{C_{11}\to C_{12}} \frac{K_{ss}}{K_{e_x}} = 0, \tag{4.12a}$$

$$\lim_{C_{44}\to 0} \frac{K_{ss}}{K_{e_x}} = \sqrt{\frac{2C_{11}}{C_{11} + 3C_{12}}}, \tag{4.12b}$$

$$\lim_{C_{11}\to C_{12}} \frac{K_{ss}}{K_{e_y}} = 0, \tag{4.12c}$$

$$\lim_{C_{44}\to 0} \frac{K_{ss}}{K_{e_y}} = \sqrt{\frac{C_{11} + C_{12}}{C_{11} + 3C_{12}}}. \tag{4.12d}$$

In the limit of $C_{11} \to C_{12}$ the ratios K_{ss}/K_{e_x} and K_{ss}/K_{e_y} go to zero. This is the origin of the apparent flattening of the right branch at the higher anisotropies. For $C_{44} \to 0$ the ratios K_{ss}/K_{e_x} and K_{ss}/K_{e_y} remain finite, explaining why the left branch remains nearly linear. Due to the complexity of the $\langle 111\rangle\{1\bar{1}0\}$ edge slip system this analytical analysis on the slope of the data cannot be carried out. However, direct examination of elastic constants shows that the branching shown in figures 1a and 2a is due to materials having low values of C_{44} (left branch) or C' (right branch): the A_c structure map is able to discern different elastic instabilities. Further examination of the numerical results in figures 4.1 and 4.2 reveal that the branching has the same origins. Hence, the structure map is able to separate compounds according to the type of instability.

In Table 4.1 the compounds in spacegroup 225 ($Fm\bar{3}m$) with the highest values of A_c^s (screw dislocation) are listed (a table of all compounds is included in the supplementary materials). This table reveals interesting trends. Many of the compounds

Table 4.1: *Listing of the compounds from spacegroup 225 that contained the highest screw anisotropy.* A_c^s *corresponds to a screw dislocation and* A_c^e *an edge dislocation.*

Compound	$A_c^s(\langle 110\rangle)$	$A_c^e(\langle 110\rangle\{111\})$	$A_c^s(\langle 111\rangle)$	$A_c^e(\langle 111\rangle\{110\})$	low modulus
$LiSiCu_2$	2.42	4.18	1.27	3.20	C'
ZrS	2.44	3.15	1.28	1.28	C_{44}
YCd_3	2.44	4.78	1.29	3.38	C'
$TiAlPd_2$	2.47	5.55	1.33	3.74	C'
$MgCdAg_2$	2.60	5.26	1.33	3.64	C'
Li_3In	2.60	4.74	1.31	3.41	C'
Li_2MgCd	2.75	5.31	1.36	3.71	C'
$AlCu_3$	2.79	5.75	1.39	3.91	C'
$LiAg_2Ge$	2.92	6.35	1.44	4.20	C'
$MnAlPd_2$	3.03	7.11	1.49	4.53	C'
$MnAlCu_2$	3.08	6.57	1.47	4.34	C'
YTe	3.11	4.07	1.48	1.47	C_{44}
Li_2ZnSn	3.14	6.03	1.45	4.16	C'
Li_3Pd	3.76	9.20	1.70	5.59	C'

contain Li or Pd. For reference, Li has the highest A_c values of all BCC materials with $A_c^s(\boldsymbol{b} = \langle 111\rangle) = 1.61$ and $A_c^s(\boldsymbol{b} = \langle 110\rangle) = 3.47$. Another observation is that alloys of similar compositions to the compounds shown in Table 4.1 are known to be shape memory alloys (SMAs). It is already known that many SMAs have a low value of C'[84, 92, 93]. Al-Cu-Mn systems are known SMAs[94]. TiPd (similar to $TiAlPd_2$) has been shown to be a high-temperature SMA[95, 96]. The emergence of the shape memory effect appears to accompany higher anisotropy in the Ti-Nb and Ti-V systems as well. For instance, Ti-(22-27) at.% Nb alloys and Ti-10V-2Fe-3Al (83.8 at.% Ti)[97] exhibit shape memory behavior[83, 93].

Two of the compounds in the table were selected for further study: $AlCu_3$ and $MnAlCu_2$. These compounds were selected because they contain relatively inexpensive materials, and if alloys with Gum-Metal-like properties can be formed at or near these compositions, they are likely to have a significant technological impact. Since Gum-Metal-like behavior emerges in the disordered solid solution phase, it is interesting to explore if solid solutions at these compositions remain elastically stable.

Elastic constants were computed using density functional theory (DFT) as implemented in the Vienna Ab initio Simulation Package (VASP) [30, 31]. The Perdew, Becke, and Ernzerhof (PBE) Generalized Gradient Approximation exchange-correlation functional was employed [32]. A plane-wave cutoff of 400 eV was used with a first-order Methfessel-Paxton smearing[98] employing a smearing parameter of 0.05

eV. Ionic relaxations were performed until all forces were less than 0.005 eV/Å. A $15 \times 15 \times 15$ Γ-centered k-point mesh was employed, which ensured that the elastic constants were converged to less than a 2% difference for $MnAlCu_2$ and a 10% difference for $AlCu_3$. To approximate a solid solution a 16-atom special quasirandom structure (SQS) [99, 100] was generated using the alloy theoretic automated toolkit (ATAT) [61]. Both pairs and triplet clusters were considered within a range of $3a_0$, a_0 being the lattice parameter associated with the (on average) BCC crystal. The elastic constants were calculated performing 4 deformations of varying magnitude for the six independent strains and after obtaining the stresses from VASP performing a linear fit [63]. The elastic constants were then symmetrized by generating the 48 transformation matrices associated with the point group of a BCC crystal and then averaging the elastic constants over the 48 transformations

$$C_{ijkl}^{sym} = \frac{1}{48} \sum_{\alpha=1}^{48} a_{ip}^{(\alpha)} a_{jq}^{(\alpha)} a_{kr}^{(\alpha)} a_{ls}^{(\alpha)} C_{pqrs}, \tag{4.13}$$

with $\boldsymbol{a}^{(\alpha)}$ corresponding to the transformation matrix of the α^{th} element of the point group. For $MnAlCu_2$ the unit cell was initialized in a ferromagnetic state.

Our calculations for the $AlCu_3$ ($D0_3$) and $MnAlCu_2$ ($L2_1$) ordered structures broadly match those generated by the materials project (see Table 4.2). For the $AlCu_3$ phase, there is a 9% difference in the values of C_{44}, which is relatively large, but not atypical for DFT calculations of the elastic constants. The $AlCu_3$ SQS structure also has noticeably different elastic constants compared to the ordered structure. Most importantly, the disordered phase is elastically unstable ($C_{11} - C_{12} < 0$). This is not surprising considering that the ordered structure is already highly elastically anisotropic, and for such materials, changes in ordering can drastically change the elastic behavior [40].

Table 4.2: *Calculated SOEC's for ordered and disordered structures of Al-Cu system as well as ordered $MnAlCu_2$. C_{11}, C_{12}, and C_{44} are all in GPa.*

Compound	$AlCu_3$[87]	$AlCu_3$	$Al_{0.25}Cu_{0.75}$	$MnAlCu_2$[87]	$MnAlCu_2$
C_{11}	147.51	158	137	138.26	140
C_{12}	122.08	117	141	116.56	123
C_{44}	99.25	108	107	103.02	105

The apparent instability of the SQS Al-Cu system complicates the computer-aided search for Gum Metal-like materials. An AlCu BCC solid solution is known to exist at temperatures above 843 K,[101] but finite temperature effects are beyond the scope of this work. However, there is an extensive literature on β-stabilizers for Al-Cu. Lanzini *et al.*[102] found the order-disorder transformation in compositions near $AlCu_3$ to be first-order and that the addition of a BCC stabilizer (Be). Fe, Mn, Ni, Sn, Be, Zn, and Cr are all known to either maintain or lower the β transition temperature for an $Al_{0.25-y}Cu_{0.75-y}X_{2y}$ system [103]. Cr has been shown to help stabilize high-entropy alloys containing Al and Cu [104]. In addition, a BCC solid solution for Al-Cu-Cr exists at 873 K [105]. A BCC solid solution exists near $Al_{0.25}Cu_{0.75}$ at similar temperatures for Al-Cu-Zn systems [106].

Since $MnAlCu_2$ in the $L2_1$ structure also displays a high anisotropy (see Table 4.1) the Al-Cu-Mn systems merit further consideration. Al-Cu-Mn systems are known SMAs.[94] At low Al compositions (less than 16 at.-% Al) the BCC phase can be stabilized at room temperature via quenching. The resulting alloy exhibits superelasticity (7.5%), high ductility (15% elongation to fracture), and a yield strength of $250 - 500$ MPa [107]. Similar to Gum Metal, low Al content Al-Cu-Mn alloys show significant cold-workability (60 - 90 % rolling reduction before cracking). In another parallel, Al-Cu-Mn, as well as Cu-Zn-Al alloys exhibit Invar behavior [108]. It is still not clear if this Invar behavior found in Al-Cu-X systems is due to the same mechanism as in Gum Metal. Al-Cu-X materials' Invar behavior appears to be a direct result of a martensitic transformation, while there exist contradictory observations for Gum Metal [6, 109]. Based on the analysis presented here and the experimental data, we hypothesize that severely cold working a disordered Al-Cu-Mn alloy with the proper composition will generate an alloy with Gum-Metal-like properties.

In conclusion, a methodology for the computational discovery of Gum-Metal-like alloys has been introduced. The method rests on the identification of a dislocation-based elastic anisotropy paramater that has been linked with the interesting behavior of Gum Metal. This parameter is then used in conjunction with data from the Materials Project to construct a structure map that allows identification of materials susceptible to Gum-Metal-like behavior, and several candidate alloys are identified. Though the identification of Gum Metals is the primary focus of the work, it is noted that the A_c structure maps may be useful for discovering and optimizing both shape memory alloys and HEAs.

Chapter 5

Approximation of the Ideal Strength of Alloys from First-Principles

The ideal strength (IS) provides the theoretical upper limit to the strength of a material and is one of the few mechanical properties of crystals that can be easily calculated using first-principles methods[110, 9, 10] and be measured experimentally [111, 112, 113, 114]. While a perfectly crystalline material does not exist in any engineering application, ideal strength calculations have been shown to be useful in numerous areas: The IS has been applied to understanding the homogeneous nucleation of dislocation under nanoindentation[115, 116, 117], the unstable propagation of a cleavage crack[118, 119], as well as the intrinsic ductility of a crystal[120, 121, 36] and the preferred cleavage plane of transition metal aluminides[122]. Perhaps most famously, the failure in Frenkel's attempt to calculate the yield strength of a crystal in terms of ideal slip [123] ultimately led to the theory of defect-mediated plasticity (DMP) [3, 2, 1]. While DMP is the predominant deformation mechanism in structural materials, IS still plays an integral role in understanding the mechanical properties of crystalline materials. This is especially relevant to the development of alloy systems over the past decade, whose yield strength is on the order of the ideal strength[6, 14].

While IS calculations for elemental or ordered crystals can be performed with relative ease, the calculation of the IS of a random solid solution using density-functional theory (DFT) continues to be problematic for several reasons. Perhaps most importantly, all IS calculations rely heavily on the symmetry of an undeformed crystal, which is not present in a random solid solution. Previous studies have used methods such as the virtual crystal approximation (VCA) or coherent potential approximation (CPA) to compute the ideal strength of solid solutions while retaining the symmetry of the crystal[8, 124]. These methods, however, fail to take into account the local configurations of the atoms in the alloy. A method is proposed, which attempts to overcome these two barriers by combining the calculation of the elastic constants of a small set of ordered structures (SSOS)[125] with nonlinear elasticity in a manner resembling that developed by Wang and Li for high symmetry structures[126].

5.1 Theory

We begin by defining the symmetric Wallace tensor, which governs the elastic stability of an anisotropic solid, as [22, 23]

$$\Lambda_{klmn} = C'_{klmn} + \frac{1}{2}\left(\tau_{km}\delta_{ln} + \tau_{kn}\delta_{lm} + \tau_{lm}\delta_{kn} + \tau_{ln}\delta_{km} - \tau_{kl}\delta_{mn} - \tau_{mn}\delta_{kl}\right). \tag{5.1}$$

Here δ_{ln} is the Kronecker-delta, τ_{km} the Second Piola-Kirchhoff stress tensor, and C'_{klmn} the second-order elastic constants of the solid under finite deformation (ECFD). C'_{klmn} is defined as

$$C'_{klmn} = \frac{1}{V(\boldsymbol{\eta})}\left(\frac{\partial^2 E}{\partial\beta_{kl}\partial\beta_{mn}}\right)_{\boldsymbol{\beta}',\boldsymbol{\eta}}, \tag{5.2}$$

with $V(\boldsymbol{\eta})$ being the volume at a finite (Green-Lagrangian) strain ($\boldsymbol{\eta}$), E the elastic energy, and $\boldsymbol{\beta}$ an infinitesimal strain applied in addition to the finite strain (See Figure 5.1 for a graphical representation). A material is elastically unstable if det $\boldsymbol{\Lambda} \leq 0$, and is said to be intrinsically ductile if the eigenvector associated with the instability has only shear components; the material fails in a manner other than the Young's modulus going to zero.

We will approximate the elastic energy using a Taylor series expansion of the elastic energy up to the the third order. It should be noted, however, that this method works for any order.

$$V_0\Delta E \approx \frac{1}{2!}C_{klmn}\eta_{kl}\eta_{mn} + \frac{1}{3!}C_{klmnpq}\eta_{kl}\eta_{mn}\eta_{pq} + ..., \tag{5.3}$$

with the second- and third-order elastic constants (SOEC and TOEC) being defined as

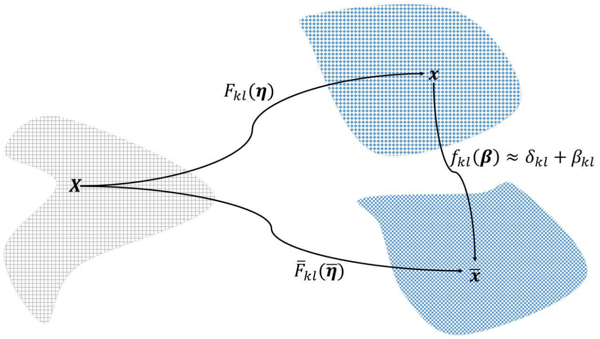

Figure 5.1: *Illustration of the three strain states considered in the derivation of* C'_{klmn}*.* $\boldsymbol{F}$ *is the deformation gradient mapping the reference configuration* ($\boldsymbol{X}$) *to the finite strain state* ($\boldsymbol{x}$)*.* $\boldsymbol{f}$ *maps* $\boldsymbol{x}$ *to* $\bar{\boldsymbol{x}}$*, which is under a combined finite and infinitesimal strain.*

$$C_{klmn} = \frac{1}{V_0}\left(\frac{\partial^2 E}{\partial\eta_{kl}\partial\eta_{mn}}\right)_{\boldsymbol{\eta}=0}, \tag{5.4a}$$

$$C_{klmnpq} = \frac{1}{V_0}\left(\frac{\partial^3 E}{\partial\eta_{kl}\partial\eta_{mn}\partial\eta_{pq}}\right)_{\boldsymbol{\eta}=0}. \tag{5.4b}$$

By combining equations 5.2 and 5.3 the elastic constants under finite deformation can be determined entirely in terms of the elastic constants and the finite strain.

Three configurations are considered in deriving the ECFD: the zero strain reference configuration ($\boldsymbol{X}$), configuration under a finite strain of $\boldsymbol{\eta}$ ($\boldsymbol{x}$), and a configuration under a combined finite and infinitesimal strain ($\bar{\boldsymbol{x}}$). These configurations can be mapped to each other by the use of deformation gradients, which are defined as

$$F_{km} = \frac{\partial x_k}{\partial X_m}, \tag{5.5a}$$

$$\bar{F}_{km} = \frac{\partial \bar{x}_k}{\partial X_m}, \tag{5.5b}$$

$$f_{km} = \frac{\partial \bar{x}_k}{\partial x_m}. \tag{5.5c}$$

The deformation gradient is related to the Green-Lagrange strain by

$$\eta_{km} = \frac{1}{2}\left(F_{pk}F_{pm} - \delta_{km}\right), \tag{5.6}$$

and can be analytically solved for entirely in terms of the strain. With $\boldsymbol{F} = \boldsymbol{F}(\boldsymbol{\eta})$ in hand we can define all configurations in terms of the applied strains[127] using equation 5.5, assuming that $\boldsymbol{f}$ can be expressed in terms of the infinitesimal strain $(\boldsymbol{\beta})$ as

$$f_{km} = \delta_{km} + \beta_{km}. \tag{5.7}$$

By substituting the Taylor series expansion of the elastic energy in terms of the combined infinitesimal and finite strain state $(\bar{\boldsymbol{\eta}})$ into the definition of the ECFD C'_{klmn} can be expressed as

$$C'_{ijkl} = \frac{1}{J(\bar{\boldsymbol{\eta}})}\left(C_{mnpq} + C_{mnpqrs}\bar{\eta}_{rs}\right)\left(\frac{\partial^2 \bar{\eta}_{mn}}{\beta_{ij}\beta_{kl}}\bar{\eta}_{pq} + \frac{\partial \bar{\eta}_{mn}}{\beta_{kl}}\frac{\partial \bar{\eta}_{pq}}{\beta_{ij}}\right), \tag{5.8}$$

where $J(\bar{\boldsymbol{\eta}}) = \det \bar{\boldsymbol{F}}$. It should be noted that equation 5.8 is similar to that determined by Wang and Li [126], but includes the term $\frac{\partial^2 \bar{\eta}_{mn}}{\beta_{ij}\beta_{kl}}\bar{\eta}_{pq}$. As $\bar{\boldsymbol{F}}$ can be determined entirely in terms of $\boldsymbol{\eta}$ and $\boldsymbol{\beta}$, equation 5.8 is completely defined in term of $\boldsymbol{\eta}$ and the elastic constants. For a uniaxial load applied along the [001] direction the ECFD are [11]

$$C'_{11} = C_{11} + \left(3C_{11} + C_{12} + C_{111} + C_{112}\right)\zeta + \left(-C_{11} + C_{12} + C_{112}\right)\xi, \tag{5.9a}$$

$$C'_{12} = C_{12} + (2C_{12} + 2C_{112})\zeta + (-C_{12} + C_{123})\xi, \tag{5.9b}$$

$$C'_{13} = C_{12} + (C_{112} + C_{123})\zeta + (C_{12} + C_{112})\xi, \tag{5.9c}$$

$$C'_{33} = C_{11} + (-2C_{11} + 2C_{12} + 2C_{112})\zeta + (4C_{11} + C_{111}), \tag{5.9d}$$

$$C'_{44} = C_{44} + \frac{1}{4}(C_{11} + 3C_{12} + 4C_{144} + 4C_{166})\zeta + \frac{1}{4}(C_{11} + C_{12} + 4C_{44} + 4C_{166})\xi, \tag{5.9e}$$

$$C'_{66} = C_{44} + \frac{1}{2}(C_{11} + C_{12} + 4C_{44} + 4C_{166})\zeta + \frac{1}{2}(C_{12} - 2C_{44} + 2C_{144})\xi. \tag{5.9f}$$

Here ζ and ξ are components of the Green-Lagrangian strain tensor such that the tensor has the form in Voigt notation $\boldsymbol{\eta} = (\zeta, \zeta, \xi, 0, 0, 0)$. Using the expansion of $\boldsymbol{\tau}$ in terms of $\boldsymbol{\eta}$ and knowing that $\tau_{11} = 0$ for a uniaxial load applied along [001], both $\boldsymbol{\eta}$ and $\boldsymbol{\tau}$ can be defined entirely by ξ.

This formalism allows for the symmetric Wallace tensor to be efficiently approximated for a solid solution. One can do this by calculating the SOEC and TOEC [11] of a special quasirandom structure (SQS)[99, 100], which in general consists of a triclinic cell, but retains the local structure of the alloy, and then symmetrizing to match the point group of the macroscopic crystal using the equations

$$C_{klmn} = \frac{1}{n_G} \sum_{\alpha=1}^{n_G} a_{kp}^{(\alpha)} a_{lq}^{(\alpha)} a_{mr}^{(\alpha)} a_{ns}^{(\alpha)} C_{pqrs}^{SQS}, \tag{5.10a}$$

$$C_{klmnpq} = \frac{1}{n_G} \sum_{\alpha=1}^{n_G} a_{kr}^{(\alpha)} a_{ls}^{(\alpha)} a_{mt}^{(\alpha)} a_{nu}^{(\alpha)} a_{pv}^{(\alpha)} a_{qw}^{(\alpha)} C_{rstuvw}^{SQS}, \tag{5.10b}$$

with n_G being the number of elements in the point group and Einstein summation notation implied. The final elastic constants are then found by performing a weighted averaging of the three highest performing SQS structures. The effective value for a general material property (f) of an alloy can be expressed as [125]

$$\langle f \rangle \approx \sum_{\beta=1}^{n_{SQS}} w_\beta f\left(\sigma_\beta^{SQS}\right), \tag{5.11}$$

with σ_β^{SQS} being the configuration of the β^{th} SQS structure and w_β being the weight for the β^{th} configuration.

5.2 Method

5.2.1 SQS Generation

SQS were generated in this work using a genetic algorithm (GA), described in detail elsewhere [128]. The optimization process starts by calculating the atomic correlation functions of a random solid solution, $\mathbf{x}^{random}$ and the vector describing the correlation functions of the finite-sized supercell $\mathbf{x}^{scell}$. The norm of the difference of $\mathbf{x}^{random}$ and $\mathbf{x}^{scell}$ is minimized in the GA optimization procedure and the fitness of any atomic configuration is inversely proportional to $\left\|\mathbf{x}^{random} - \mathbf{x}^{scell}\right\|$.

In total 4 pair correlation functions are considered, which correspond to a cut-off distance r of $r < 1.7a$, where a represents the lattice constant of the BCC conventional cell. In addition, 4 triplet correlation functions are used. These are selected such that no triplets contain pairs longer than $1.42a$. The point correlations are implicitly imposed by specifying an alloy composition. These remain fixed during the GA optimization process, and hence require no further consideration. The atomic correlation functions of a large collections of SQS cells are computed in every GA iteration using the alloy theoretic automated toolkit (ATAT) [129, 130, 61] and fed back into the GA for further optimization. Higher weights were assigned to the atomic correlations functions corresponding to short distances and higher multiplicities, given their higher anticipated contributions to total energies and elastic constants of SQS. The result of varying these weights however, was found to have only a small impact on the final optimized SQS.

5.2.2 Generation of TOEC

Below is an outline of the method used to calculate the third-order elastic constants [11].

The third-order elastic constants are defined as

$$C_{ijklmn} = \rho_0 \frac{\partial^3 E}{\partial \eta_{ij} \partial \eta_{kl} \partial \eta_{mn}} |_{\boldsymbol{\eta}=0}. \tag{5.12}$$

Using Voigt notation this can be written as

$$C_{ijk} = \rho_0 \frac{\partial^3 E}{\partial \eta_i \partial \eta_j \partial \eta_k} |_{\boldsymbol{\eta}=0}. \tag{5.13}$$

If the TOEC contains Voigt symmetry, but no point symmetry other than the identity, the sixth-order elastic tensor will consist of 56 unique constants. By evaluating the second derivative of the stress components with respect to η for 14 unique strain states defined as

$$\boldsymbol{\eta}^1 = \begin{pmatrix}\eta & 0 & 0 & 0 & 0 & 0\end{pmatrix}, \tag{5.14a}$$
$$\boldsymbol{\eta}^2 = \begin{pmatrix}0 & \eta & 0 & 0 & 0 & 0\end{pmatrix}, \tag{5.14b}$$
$$\boldsymbol{\eta}^3 = \begin{pmatrix}0 & 0 & \eta & 0 & 0 & 0\end{pmatrix}, \tag{5.14c}$$
$$\boldsymbol{\eta}^4 = \begin{pmatrix}0 & 0 & 0 & 2\eta & 0 & 0\end{pmatrix}, \tag{5.14d}$$
$$\boldsymbol{\eta}^5 = \begin{pmatrix}0 & 0 & 0 & 0 & 2\eta & 0\end{pmatrix}, \tag{5.14e}$$
$$\boldsymbol{\eta}^6 = \begin{pmatrix}0 & 0 & 0 & 0 & 0 & 2\eta\end{pmatrix}, \tag{5.14f}$$
$$\boldsymbol{\eta}^7 = \begin{pmatrix}\eta & \eta & 0 & 0 & 0 & 0\end{pmatrix}, \tag{5.14g}$$
$$\boldsymbol{\eta}^8 = \begin{pmatrix}\eta & 0 & \eta & 0 & 0 & 0\end{pmatrix}, \tag{5.14h}$$
$$\boldsymbol{\eta}^9 = \begin{pmatrix}\eta & 0 & 0 & 2\eta & 0 & 0\end{pmatrix}, \tag{5.14i}$$
$$\boldsymbol{\eta}^{10} = \begin{pmatrix}\eta & 0 & 0 & 0 & 2\eta & 0\end{pmatrix}, \tag{5.14j}$$
$$\boldsymbol{\eta}^{11} = \begin{pmatrix}0 & \eta & \eta & 0 & 0 & 0\end{pmatrix}, \tag{5.14k}$$
$$\boldsymbol{\eta}^{12} = \begin{pmatrix}0 & 0 & 0 & 2\eta & 2\eta & 0\end{pmatrix}, \tag{5.14l}$$
$$\boldsymbol{\eta}^{13} = \begin{pmatrix}0 & 0 & 0 & 2\eta & 0 & 2\eta\end{pmatrix}, \tag{5.14m}$$
$$\boldsymbol{\eta}^{14} = \begin{pmatrix}0 & 0 & 0 & 0 & 2\eta & 2\eta\end{pmatrix}. \tag{5.14n}$$

results in a vector, $\boldsymbol{\tau}$, containing 84 terms that consist of the 56 TOEC. Writing the TOEC as a 56×1 array, $\boldsymbol{\xi}$, the 84×56 matrix, $\boldsymbol{A}$, can be defined as

$$A_{ik} = \frac{\partial \tau_i}{\partial \xi_k} \tag{5.15}$$

Defining $\boldsymbol{B}$ to be the pseudoinverse of $\boldsymbol{A}$ the TOEC can be defined as

$$\xi_i = B_{ik}\tau_k \tag{5.16}$$

The components of $\boldsymbol{\tau}$ were evaluated numerically using the finite difference method. A 9 point central difference stencil about $\eta = 0$ was used to calculate the second derivative of the 2nd Piola-Kirchhoff stress components. While the maximum strain used in the finite difference calculations is system dependent and determined from convergence testing with respect to the TOEC, a maximum strain of $\eta_{max} = 0.05$ has been shown to be appropriate for most systems studied.

5.2.3 Computational Details

We performed elastic constants calculations using density functional theory (DFT) as implemented in the Vienna Ab initio Simulation Package (VASP) [30, 31]. The

Perdew, Becke, and Ernzerhof (PBE) Generalized Gradient Approximation exchange-correlation functional was employed [32]. A plane-wave cutoff of 600 eV was used with a first-order Methfessel-Paxton smearing [98] employing a smearing parameter of 0.2 eV. Ionic relaxations were performed until all forces were less than 0.005 eV/Å. A 10 × 10 × 10 Γ-centered k-point mesh was employed. To ensure that the elastic constants were converged calculations were run with a $14 \times 14 \times 14$ Γ-centered k-point mesh for one SQS at each composition. SOEC were within 2% for the two meshes, while TOEC were found to be within a range of $1 - 25\%$. In all cases the lower and higher density k-point mesh predicted the same elastic instability. In the case of V, a 25 × 25 × 25 Γ-centered k-point mesh was employed for both SOEC and TOEC calculations. The SOEC and TOEC were calculated following the approach outlined by de Jong *et al.* [63, 11]. The SOEC and TOEC were calculated for the following 16 atom supercells: V, Ti_6V_{10}, Ti_7V_9, Ti_8V_8, Ti_9V_7, and $Ti_{10}V_6$. The TOEC were calculated for the three best elastically stable SQS cells at each structure. Both an arithmetic as well as a weighted mean of the elastic constants using the SSOS method (see equation 5.11) were calculated and considered to represent the elastic properties of the bulk random alloy.

Results

Comparing V results between reference [8] and the current work shown in Figure 5.2, a 35% difference in the ideal tensile strength σ_{ITS} is observed. This is a noticeable difference, but not necessarily unexpected as only the SOEC and TOEC are included in the expansion of the elastic energy. The inclusion of higher-order terms would likely decrease this difference, but at a much higher computational cost. Most importantly, V appears to fail via a shear instability for both methods; specifically $C'_{66} \to 0$. Examining the SQS cells, one sees the general decrease of the σ_{ITS} with increasing Ti content in agreement with VCA results. The exception to this trend are $Ti_{10}V_6$ cells.

There are several possible reasons for this, the first being that as Ti content is increased the material becomes more elastically anisotropic, leading to higher variation in the elastic properties of SQS cells depending on configuration, meaning that perhaps more SQS cells than just three are needed to accurately quantify the properties of the random alloy. Another possible reason for the bump in σ_{ITS} at $Ti_{10}V_6$ is that the material has undergone the ductile-to-brittle transition (see Figure 5.3). As shear instabilities occur at lower strains and thus lower σ_{ITS}, this would mean that even though the elastic constants might be softer, a larger strain can be applied leading to a higher σ_{ITS}.

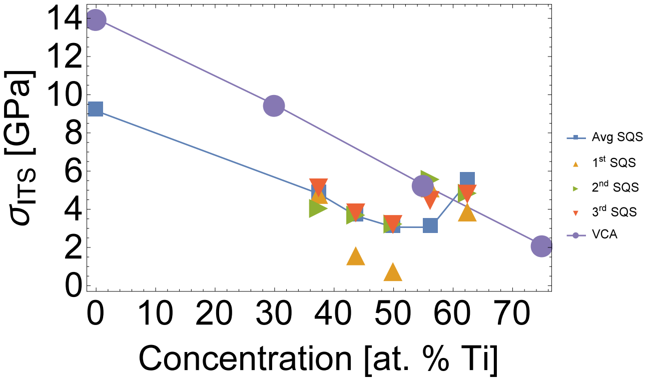

Figure 5.2: *Comparison of ideal tensile strength of Ti-V systems calculated using VCA [8] and from nonlinear elasticity. The results for the three best SQS cells are shown along with their mean.*

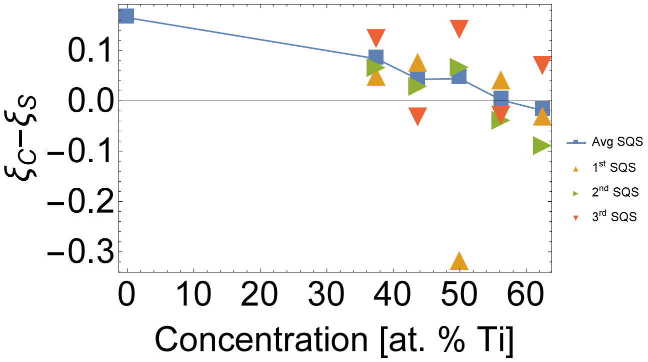

Figure 5.3: *Estimation of the ductile-to-brittle transition for the Ti-V system. The results for the three best SQS cells are shown along with their mean.* ξ_C *is the strain at which cleavage failure is predicted to occur and* ξ_S *is the strain at which ductile failure is predicted to occur (specifically* $C'_{66} = 0$*). A ductile-to-brittle transition appears at approximately 55 at % Ti in agreement with the VCA prediction [8].*

While the method described in this work appears to consistently underestimate σ_{ITS} compared to VCA, it does appear to accurately reproduce the ductile-to-brittle transition. VCA predicts that the ductile-to-brittle transition occurs at 55 at. % Ti. The current work shows the difference between the onset of a shear instability and cleavage instability occur at nearly simultaneous strains for the Ti_9V_7 system (56.25 at. % Ti). It should be noted that while the difference between the strains at the cleavage and shear strain instabilities ($\xi_C - \xi_S$) decreases with increasing Ti content the behavior of the individual SQS cells is more dispersed. The most obvious example of this is the best SQS for the 50 at. % Ti cell, which shows the largest difference in shear and cleavage instability of all cells considered.

5.3 Discussion

The fact that the σ_{ITS} predicted from this work is lower than that calculated by VCA is not all together surprising. A major advantage of this method is that the effects of local configurations of atoms in the alloy are implicitly included in the elastic constants. It is possible that the incorporation of these local contributions could lead to a lower σ_{ITS}. However, elastic constants higher than TOEC should be included in this calculation to test this idea further. Higher order terms would most definitely lead to a more accurate model of the ideal strength, but at a much higher cost; a triclinic cell has at most 21 SOEC, 56 TOEC, and 126 fourth-order elastic constants.

In addition to modeling the intrinsic ductile-to-brittle transition this model can in principle be applied to determine the ideal yield surface of an alloy for any type of applied strain state. Although, depending on the system higher order terms in the elastic constants might be necessary for more complex stress-strain relations such as those seen in transition metal aluminides [122, 131]. If applicable, this offers a tremendous savings in calculations for understanding both the intrinsic ductility as well as strength as a function of orientation, without needing any further ideal strength calculations.

Chapter 6

Ideal Tensile Yield Surface of a Crystal

The computational cost of calculating the ideal strength of a material using DFT can vary widely. For instance, the calculation of the ideal tensile strength of a cubic system under an uniaxial load is a relatively simple computation. However, the costs can increase dramatically for lower symmetry structures and/or high index orientations. In addition, data obtained from the IS calculation for one configuration in a crystal cannot be used to speed up the IS calculation for another configuration. As a result, a calculation such as the ideal tensile yield surface of a cubic crystal is an impractical venture.

However, by approximating the elastic stability of a crystal with nonlinear elasticity theory, the ideal yield surface for any applied load becomes easily accessible. There is an upfront computation cost in terms of calculating the higher-order elastic constants, but for high symmetry structures this is on the order of the computation cost associated with the ideal tensile strength of the material along the $\langle 001 \rangle$ direction. In this chapter, it is shown how one can generalize the method introduced in chapter 5 to create the ideal tensile yield surface of a material. This method works by first, defining the form of the applied load (in this case it is uniaxial) and then expanding the Green-Lagrangian strain in terms of the applied stress, so that the symmetric Wallace tensor can be constructed.

To test this method, the ideal tensile and compressive yield surfaces of copper are constructed both with and without fourth-order elastic constants. It is shown that, provided accurate elastic constants are used, this model reproduces the maxima and minima tensile load directions in Cu predicted from direct IS calculations in DFT in addition to correctly predicting the form of the eigenstrain associated with failure.

6.1 Theory

6.1.1 Stress-strain Relations

For an arbitrary orientation, the strain state associated with the uniaxial load (written in terms of the second Piola-Kirchhoff stress as $\tau_{km} = \tau_0 \delta_{k3} \delta_{m3}$) will be complex due to the lack of symmetry. As the formalism developed in chapter 5 uses strain as an input, a general relationship between the stress and strain needs to be approximated. To account for this the strain is approximated in terms of the stress using the elastic compliance tensors ($\boldsymbol{D}$) [132]. To begin the derivation, the elastic energy must be written as a Taylor series expansion in terms of either the stress or strain,

$$E = \frac{1}{2!} D_{ijkl} \tau_{ij} \tau_{kl} + \frac{1}{3!} D_{ijklmn} \tau_{ij} \tau_{kl} \tau_{mn} + \frac{1}{4!} D_{ijklmnpq} \tau_{ij} \tau_{kl} \tau_{mn} \tau_{pq} + \ldots, \tag{6.1a}$$

$$E = \frac{1}{2!} C_{ijkl} \eta_{ij} \eta_{kl} + \frac{1}{3!} C_{ijklmn} \eta_{ij} \eta_{kl} \eta_{mn} + \frac{1}{4!} C_{ijklmnpq} \eta_{kl} \eta_{ij} \eta_{mn} \eta_{pq} + \ldots \tag{6.1b}$$

The compliance tensors $\boldsymbol{D}$ can be determined by taking into account the fact that

$$\frac{\partial \tau_{ij}}{\partial \tau_{kl}} = I_{ijkl}, \tag{6.2a}$$

$$\frac{\partial^2 \tau_{ij}}{\partial \tau_{kl} \partial \tau_{mn}} = 0, \tag{6.2b}$$

$$\frac{\partial^3 \tau_{ij}}{\partial \tau_{kl} \partial \tau_{mn} \partial \tau_{pq}} = 0, \tag{6.2c}$$

$$\tag{6.2d}$$

where I_{ijkl} is the fourth-order identity tensor; $I_{ijkl} = \frac{1}{2} \left(\delta_{ik} \delta_{jl} + \delta_{il} \delta_{jk} \right)$. As both the compliance tensors and the elastic constants are evaluated at the stress free and strain free states, the compliance tensors are defined by differentiating the expansion of the elastic energy,

$$\frac{\partial^2 E}{\partial \tau_{ij} \partial \tau_{kl}} = D_{ijkl}, \tag{6.3a}$$

$$\frac{\partial^3 E}{\partial \tau_{ij} \partial \tau_{kl} \tau_{mn}} = D_{ijklmn}, \tag{6.3b}$$

$$\frac{\partial^4 E}{\partial \tau_{ij} \partial \tau_{kl} \tau_{mn} \tau_{pq}} = D_{ijklmnpq}. \tag{6.3c}$$

By substituting equations 6.3 into the derivatives of $\boldsymbol{\tau}$ ($\tau_{ij} = \frac{\partial E}{\partial \eta_{ij}}$) with respect to $\boldsymbol{\tau}$, the compliance tensors can be found in terms of the elastic constants,

$$D_{ijkl} = C^{-1}_{ijkl}, \tag{6.4a}$$

$$D_{ijklmn} = -D_{ijpq} C_{pqrsuv} D_{rskl} D_{uvmn}, \tag{6.4b}$$

$$D_{ijklmnpq} = D^{\alpha}_{ijklmnpq} + D^{\beta}_{ijklmnpq} \tag{6.4c}$$

$$D^{\alpha}_{ijklmnpq} = -D_{pqab} D_{cdij} D_{efkl} D_{ghmn} C_{abcdefgh}, \tag{6.4d}$$

$$D^{\beta}_{ijklmnpq} = -D_{pqab} C_{abcdef} (D_{cdijmn} D_{efkl} + D_{efklmn} D_{cdij} + D_{cdijkl} D_{efmn}), \tag{6.4e}$$

which then allow for the strain to be written in terms of the stress,

$$\eta_{ij} = D_{ijkl} \tau_{kl} + \frac{1}{2!} D_{ijklmn} \tau_{kl} \tau_{mn} + \frac{1}{3!} D_{ijklmnpq} \tau_{kl} \tau_{mn} \tau_{pq} + ... \tag{6.5}$$

6.1.2 General Ideal Tensile Calculation

Now that it is possible to approximate the applied strain for any stress, the ideal tensile yield surface can be constructed. This consists of multiple steps. A direction $\langle uvw \rangle$, along which the uniaxial load will be applied, is chosen. Then a transformation matrix is constructed that maps the original reference frame (defined by the 3 orthonormal vectors $\boldsymbol{e}_i$) to the current reference frame (defined by the 3 orthonormal vectors $\boldsymbol{e}'_i$ where $\boldsymbol{e}'_3$ is along $\langle uvw \rangle$). The stress tensor associated with the uniaxial load in the current reference frame can then be defined as $\tau_{ij} = \tau_0 \delta_{i3} \delta_{j3}$ and rotated into the original reference frame.

At this point the symmetric Wallace tensor can be constructed by entering the stress tensor into equation 6.5. For a cubic system the ECFD are defined in chapter 5 only in terms of the SOEC's and TOEC's. Including the FOEC's greatly increases the complexity of the ECFD. However, the derivation remains exactly the same as that described in the previous chapter. By rotating the symmetric Wallace tensor into the current reference frame, one can solve for the stress (either compressive or tensile) needed to initiate an elastic instability ($\det \mathbf{\Lambda} = 0$). To obtain the Cauchy stress associated with failure, $\boldsymbol{\sigma}$, its relation with the second Piola-Kirchhoff stress tensor is used,

$$\sigma_{ij} = \frac{1}{J} F_{ik} \tau_{kl} F_{jl}, \tag{6.6}$$

with J being the Jacobian, which is defined as $J = \det \boldsymbol{F}$.

The mode of this instability (shear or cleavage) can then be found by determining the eigenvector associated with the instability. The intrinsic ductility for the uniaxial load along an arbitrary direction can be assessed by calculating the Young's modulus for the particular orientation. If the Young's modulus causes the elastic instability, the material is said to be intrinsically brittle. A more computationally inexpensive way to determine if the material failed in an intrinsically brittle manner is to view the η_3 component of the eigenstrain associated with the elastic instability. If it is equal to zero then a shear instability occurred. Otherwise, the material failed in an intrinsically brittle manner. Throughout this chapter the η_3 component of the eigenstrain associated with the elastic instability will be referred to as a measure of intrinsic brittleness (IB).

6.2 Results

The elastic constants (SOEC's, TOEC's, and FOEC's) used in this study were calculated by Wang and Mo [133]. The specific values are shown in tables 6.1, 6.2, and 6.3. The yield surface was generated by evaluating 181 equispaced points with respect to the stereographic projection on the irreducible wedge of cubic system. The ideal compressive and tensile strengths were calculated at each of the points as well as the IB for both load types.

Table 6.1: *SOEC of Cu used in the calculation of the ideal yield surface. All values are in GPa.*

C_{11}	C_{12}	C_{44}
168	114	74.5

Figure 6.1 compares the ideal tensile yield strength calculated with and without FOEC's. Qualitatively comparing the two yield surfaces one sees little difference. Both approximations predict that the ⟨110⟩ direction to be the weakest tension and

Table 6.2: *TOEC of Cu used in the calculation of the ideal yield surface. All values are in GPa.*

C_{111}	C_{112}	C_{123}	C_{144}	C_{166}	C_{456}
-1500	-970	-71	-7	-901	45

Table 6.3: *FOEC of Cu used in the calculation of the ideal yield surface. All values are in GPa.*

C_{1111}	C_{1112}	C_{1122}	C_{1123}	C_{1144}	C_{1155}	C_{1255}	C_{1166}	C_{1456}	C_{4444}	C_{4455}
11900	6830	6600	-98	135	6630	-308	5740	-417	5090	-191

the $\langle 111 \rangle$ direction to be the strongest. Further, the numerical values for both maxima and minima are similar. The smallest value of σ_{ITS} over the surface was 3.32 and 4.94 with and without FOEC's, while the highest value of σ_{ITS} over the surface was 12.7 and 12.3 with and without FOEC's.

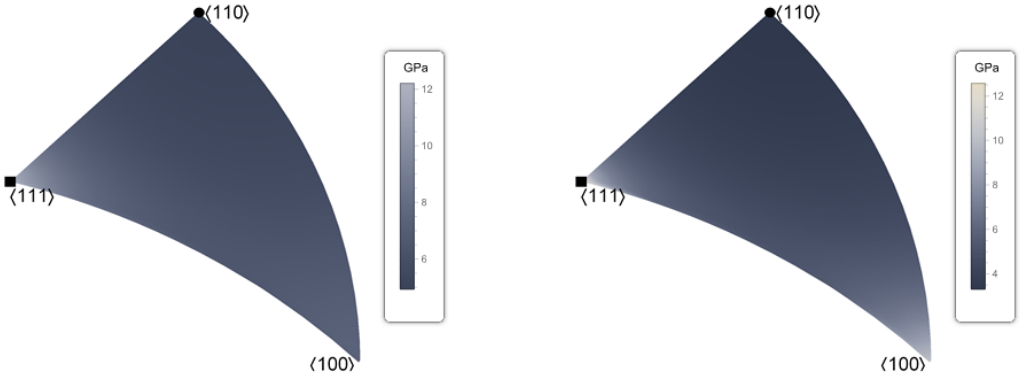

a) b)

Figure 6.1: *The ideal tensile yield surface of Cu plotted over the irreducible wedge of a cubic system. Figure a shows the yield surface including only SOEC's and TOEC's. Figure b includes the FOEC's. The filled circle and square correspond to the smallest and highest ideal yield strength on the yield surface respectively.*

As shown in Table 6.4, the results of this work both with and without FOEC's included compare well to the literature values for ideal tensile strength calculations along the high symmetry directions. In the $\langle 001 \rangle$ direction the nonlinear elasticity calculation differs from the direct DFT result by 21% and 10% with and without FOEC's, while for the $\langle 011 \rangle$ direction the difference is 36% and 5%. Finally, the nonlinear elasticity results differ from DFT in the $\langle 111 \rangle$ directions by 37% and 39%.

While the results can differ from DFT, especially in the case of ⟨111⟩ the ordering the yield strengths is consistent between DFT and the nonlinear elasticity calculations.

Table 6.4: *Comparison of ideal yield strength for high symmetry directions (⟨001⟩, ⟨110⟩, and ⟨111⟩) with literature. Under the method column DFT refers to the calculation of the ITS directly from DFT.*

σ_{ITS}	Direction	Instability	Method
Tension			
7.38	⟨001⟩	$C_{11} - C_{12}$	no FOEC
4.94	⟨011⟩	Cleavage	no FOEC
12.3	⟨111⟩	Cleavage	no FOEC
10.4	⟨001⟩	$C_{11} - C_{12}$	w/FOEC
3.31	⟨011⟩	Cleavage	w/FOEC
12.7	⟨111⟩	Cleavage	w/FOEC
9.4	⟨001⟩	$C_{11} - C_{12}$	DFT [134]
5.2	⟨011⟩	Cleavage	DFT [135]
20.3	⟨111⟩	Cleavage	DFT [135]
Compression			
3.78	⟨001⟩	Cleavage	no FOEC
15.2	⟨011⟩	Cleavage	no FOEC
20.9	⟨111⟩	Cleavage	no FOEC
3.23	⟨001⟩	C_{66}	w/FOEC
7.15	⟨011⟩	Cleavage	w/FOEC
16.0	⟨111⟩	Cleavage	w/FOEC
3.5	⟨001⟩	Cleavage	DFT[134]

For the compressive ideal yield strength (Figure 6.2), again, one sees qualitative agreement between the two approximations. The surface including FOEC's has the same maximum and minimum σ_{ITS} as that excluding FOEC's. However, one does see a larger difference in the actual values of the yield strength as a function of direction. For instance, σ_{ITS} at ⟨111⟩ is 16.0 with FOEC's and 20.9 without. Comparing these results to the literature, for the ⟨001⟩ direction the calculation without FOEC's appears to be closer in value to DFT results than the calculations with FOEC's. Combining this observations with those from the tensile case, it is not apparent that the increased complexity inherent to including higher-order terms results in any increase in accuracy. This is most likely due to the great difficulty in accurately determining the FOEC's.

Comparing the results of intrinsic brittleness for tensile loads (Figure 6.3) no

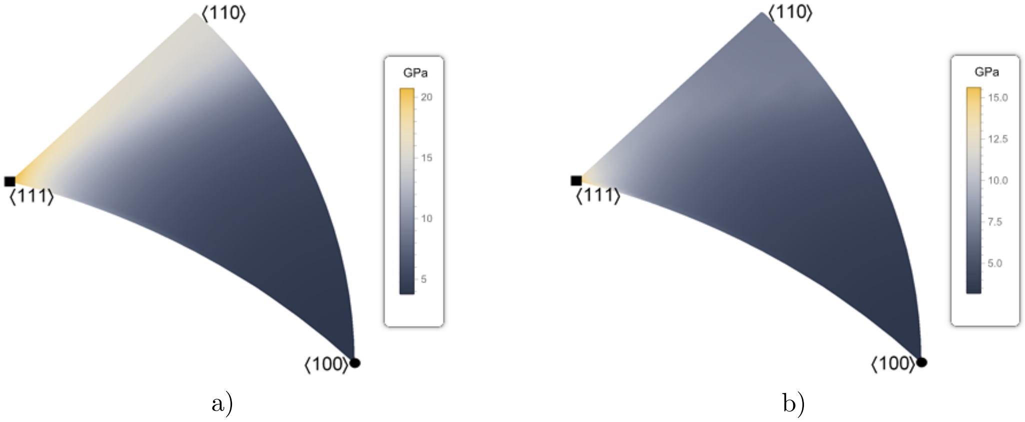

Figure 6.2: *The ideal compressive yield surface of Cu plotted over the irreducible wedge of a cubic system. Figure a shows the yield surface including only SOEC's and TOEC's. Figure b includes the FOEC's. The filled circle and square correspond to the smallest and highest ideal yield strength on the yield surface respectively.*

apparent difference is seen from including FOEC's. Both approximations predict cleavage where DFT predicts cleavage and both methods predict failure via a shear instability ($C_{11} - C_{12}$) for $\langle 001 \rangle$ in agreement with DFT calculations. In the case of a compressive load, a larger discrepancy is seen between the two approximations as shown in Figure 6.4. The yield surface without FOEC's predicts that Cu is intrinsically brittle over the entire surface while the inclusion of FOEC leads to intrinsic ductility at $\langle 001 \rangle$ with the material failing via $C_{66} \to 0$. It appears that including only SOEC's and TOEC's in the calculation is actually more accurate as, using the only data point available in the literature, DFT predicts that a compressive load along $\langle 001 \rangle$ will result in cleavage of the crystal.

6.3 Discussion

To generalize this concept further, any material pulled along a direction not associated with an axis of symmetry in the crystal must be intrinsically brittle. This can be confirmed, again, by viewing the eigenstrains associated with the symmetric Wallace tensor, which all contain some finite η_3 component.

This is not altogther too surprising a finding, as the description of intrinsic ductility has since its inception been intimately related to symmetry. For instance, the shear instability C_{66} seen in vanadium, niobium, and tantalum is often explained as a

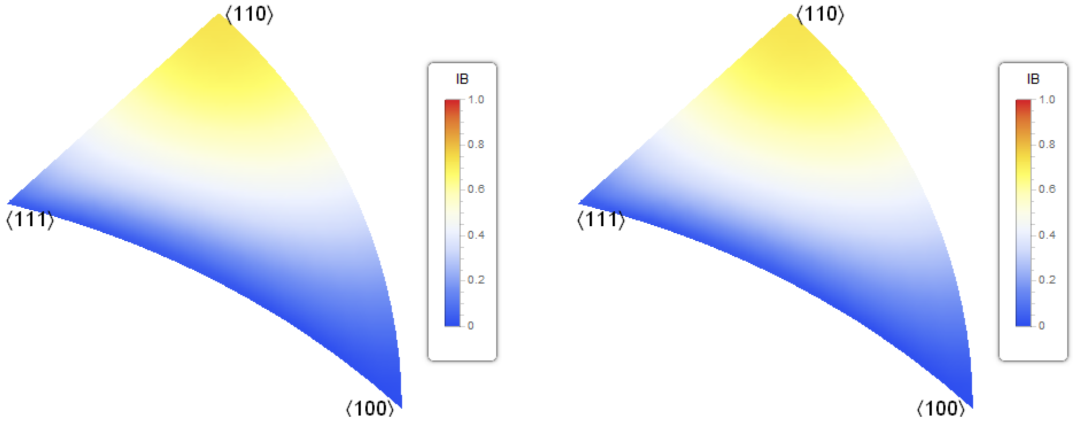

a) b)

Figure 6.3: *The ideal brittleness measurement for an applied tensile load of Cu plotted over the irreducible wedge of a cubic system. Figure a shows the yield surface including only SOEC's and TOEC's. Figure b includes the FOEC's.*

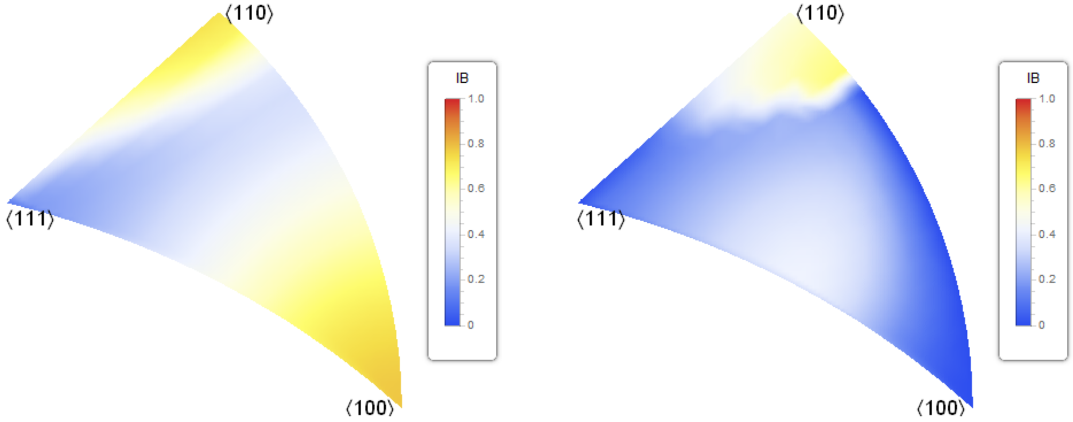

a) b)

Figure 6.4: *The ideal brittleness measurement for an applied compressive load of Cu plotted over the irreducible wedge of a cubic system. Figure a shows the yield surface including only SOEC's and TOEC's. Figure b includes the FOEC's.*

transformation from a body-centered-tetragonal (BCT) structure to an face-centered-orthorhombic (FCO) structure [36, 121, 66, 33]. This is only possible because the loaded crystal contains a high enough symmetry for it to be possible for the crystal to transform into a different crystal class (BCT or FCO). For low symmetry structures this is not possible. The crystal has only one possible path to follow, which necessitates that it fails via cleavage (the Young's modulus reaches 0).

Chapter 7

Conclusion

The goal of this research has been to develop and implement a methodology for the computer-aided materials design of Gum Metal-like alloys. The attempts at achieving this goal began with attempting to find Gum Metal-like behavior in magnesium and lithium-magnesium alloys by tuning the elastic properties of the material with respect to pressure and lithium content. In the case of tuning with respect to pressure, as the pressure was reduced from the region of absolute stability for the BCC phase, dislocation core spreading occurred, leading to structures resembling nanodisturbances. Ideal tensile strength calculations of BCC Mg as a function of pressure showed that despite its low shear modulus, BCC Mg was predicted to be intrinsically brittle at absolute zero.

In the case of lithium-magnesium alloys, a softening of the shear modulus, $C_{11} - C_{12}$, and the acoustic phonon branch between the Γ and N high symmetry points took place, as the composition approaches the stability limit for the BCC phase. Nanodisturbances appeared in conjunction with this softening as in the case of high pressure magnesium. Again, ideal tensile strength calculations predicted that ordered phases of lithium-magnesium alloys were intrinsically brittle.

In order to generalize this method further an anisotropy parameter associated with the susceptibility of dislocations to pinning was modified to be applicable to any straight dislocation in any crystal system. Using the Materials Project's elastic constants database several candidate Gum Metals were identified. Many of these materials already bear numerous striking resemblances to Gum Metal, including Al-Cu-Mn solid solutions. In addition, it is noted that the approach may be suitable for discovery and optimization of both shape memory and high entropy alloys.

Finally, in order to evaluate the intrinsic ductility of these candidate materials a method was developed to approximate the elastic stability of random alloy by a combination of nonlinear elasticity theory and special quasirandom structures. Using BCC Ti-V system as a test case, it was shown that the ductile-to-brittle transition can be accurately calculated for this system. The approach was further generalized to allow for the calculation of the ideal tensile surface of a solid.

Using what has been learned from this work, three projects appear to be of utmost interest. The first, is to further investigate the candidacy of Al-Cu-Mn for gum-metal-like behavior. To begin with, it would be of interest to calculate the intrinsic ductility of the Al-Cu-Mn compositions of interest using the methodology outlined in chapter 5. This would not necessarily be a simple calculation due to the relatively large system needed to approximate the compositions of interest (around 30-50 atoms would likely be needed). In addition to this Al-Cu-Mn alloys are known to be ferromagnetic and the BCC phase at room temperature is only achieved after quenching, leading to the possiblity that it is elastically unstable at absolute zero, where DFT calculations are conducted. Experimental work on these Al-Cu-Mn systems is a more important and likely more promising approach to take, in understanding these alloys' connection to Gum Metal. One possible experiment to conduct is to cold-work the material as close to its limit as dictated by its cold-workability (60-90 % reduction in area) and then measure its stress-strain curve.

A second project to pursue is to calculate the anisotropy parameter described in chapter 4 for all structures in the Materials Project's elastic constants database. Only cubic materials were considered in this work, but structure maps described in this work were designed such that they could be made for any straight dislocation in any crystal system. As well, the number of materials in the elastic constants database has more than doubled since this work began, meaning that there are thousands more materials that can be evaluated.

Finally, the suggestion that the anisotropy parameter described in this work could be used as a descriptor of strong and tough HEAs merits further consideration. Much computational work can be done to further exam this claim. For starters, using the SSOS method the total energy calculations of five component HEAs can be efficiently and accurately computed [125]. It should be trivial then to calculate the elastic constants for these five-component systems, allowing for an efficient determination of their anisotropy parameter.

Bibliography

[1] G. I. Taylor. The mechanism of plastic deformation of crystals. part I. theoretical. P. Roy. Soc. Lond. A Mat., 145:362–387, 1934.

[2] M. Polanyi. Über eine Art Gitterstörung, die einen Kristall plastisch machen könnte. Z. Phys., 89:660–664, 1934.

[3] E. Orowan. Zur kristallplastizität. I. Z. Phys., 89:605–613, 1934.

[4] J. Allison, M. Li, C. Wolverton, and X. Su. Virtual aluminum castings: An industrial application of ICME. JOM, 58:28–35, 2006.

[5] G. B. Olson and C. J. Kuehmann. Materials genomics: From CALPHAD to flight. Scr. Mater., 70:25–30, 2014.

[6] T. Saito, T. Furuta, J.-H. Hwang, S. Kuramoto, K. Nishino, N. Suzuki, R. Chen, A. Yamada, K. Ito, Y. Seno, T. Nonaka, H. Ikehata, N. Nagasako, C. Iwamoto, Y. Ikuhara, and T. Sakuma. Multifunctional Alloys Obtained via a Dislocation-Free Plastic Deformation Mechanism. Science, 300:464–467, 2003.

[7] H. Ikehata, N. Nagasako, T. Furuta, A. Fukumoto, K. Miwa, and T. Saito. First-principles calculations for development of low elastic modulus Ti alloys. Phys. Rev. B, 70:1–8, 2004.

[8] T. Li, J. W. Morris, N. Nagasako, S. Kuramoto, and D. C. Chrzan. “ideal” engineering alloys. Phys. Rev. Lett., 98:105503, 2007.

[9] D. Roundy, C. R. Krenn, M. L. Cohen, and J. W. Morris. Ideal shear strengths of fcc aluminum and copper. Phys. Rev. Lett., 82:2713–2716, 1999.

[10] S. Ogata, J. Li, and S. Yip. Ideal pure shear strength of aluminum and copper. Science, 298:807–811, 2002.

[11] M. de Jong, I. S. Winter, D. C. Chrzan, and M. Asta. Phys. Rev. B (under review), 2017.

[12] D. C. Chrzan, M. P. Sherburne, Y. Hanlumyuang, T. Li, and J. W. Morris. Spreading of dislocation cores in elastically anisotropic body-centered-cubic materials: The case of gum metal. Phys. Rev. B, 82:184202, 2010.

[13] C. A. Sawyer, J. W. Morris, and D. C. Chrzan. Dislocation core radii near elastic stability limits. Phys. Rev. B, 87:134106, 2013.

[14] S. Kuramoto, T. Furuta, N. Nagasako, and Z. Horita. Lattice softening for producing ultrahigh strength of iron base nanocrystalline alloy. Appl. Phys. Lett., 95:1–4, 2009.

[15] G. V. Sin'ko and N. A. Smirnov. Ab initio calculations for the elastic properties of magnesium under pressure. Phys. Rev. B, 80:104113, 2009.

[16] A. K. McMahan and J. A. Moriarty. Structural phase stability in third-period simple metals. Phys. Rev. B, 27:3235–3251, 1983.

[17] M. Y. Gutkin, T. Ishizaki, S. Kuramoto, and I. A. Ovid'ko. Nanodisturbances in deformed Gum Metal. Acta Mater., 54:2489–2499, 2006.

[18] G. V. Sin'ko. Ab initio. Phys. Rev. B, 77:104118, 2008.

[19] T. Tsuchiya and K. Kawamura. Systematics of elasticity: Ab initio study in B1-type alkaline earth oxides. J. Chem. Phys., 114:10086–10093, 2001.

[20] W. Luo, D. Roundy, M. L. Cohen, and J. W. Morris. Ideal strength of bcc molybdenum and niobium. Phys. Rev. B, 66:094110, 2002.

[21] D. Roundy, C. R. Krenn, M. L. Cohen, and J. W. Morris. The ideal strength of tungsten. Philos. Mag. A, 81:1725–1747, 2001.

[22] Duane C Wallace. Thermodynamics of Crystals. Courier Corporation, 1998.

[23] W. Morris Jr and C. R. Krenn. The internal stability of an elastic solid. Philos. Mag. A, 80:2827–2840, 2000.

[24] C R Krenn, D Roundy, J W Morris, and Marvin L Cohen. Ideal strengths of bcc metals. Mater. Sci. Eng. A, 319:111–114, 2001.

[25] M. S. Daw. Elasticity effects in electronic structure calculations with periodic boundary conditions. Comput. Mater. Sci., 38:293 – 297, 2006.

[26] N. Lehto and S. Öberg. Effects of dislocation interactions: Application to the period-doubled core of the 90° partial in silicon. Phys. Rev. Lett., 80:5568–5571, 1998.

[27] V. Vítek, R. C. Perrin, and D. K. Bowen. The core structure of $\frac{1}{2}(111)$ screw dislocations in b.c.c. crystals. Philos. Mag., 21:1049–1073, 1970.

[28] C.S. Hartley and Y. Mishin. Characterization and visualization of the lattice misfit associated with dislocation cores. Acta Mater., 53:1313 – 1321, 2005.

[29] C. S. Hartley and Y. Mishin. Representation of dislocation cores using Nye tensor distributions. Mater. Sci. Eng. A, 400–401:18 – 21, 2005.

[30] G. Kresse and J. Furthmüller. Efficient iterative schemes for ab initio total-energy calculations using a plane-wave basis set. Phys. Rev. B, 54:11169–11186, 1996.

[31] G. Kresse and J. Hafner. Ab initio. Phys. Rev. B, 47:558–561, 1993.

[32] J. P. Perdew, K. Burke, and M. Ernzerhof. Generalized gradient approximation made simple. Phys. Rev. Lett., 77:3865–3868, 1996.

[33] F. Milstein and S. Chantasiriwan. Theoretical study of the response of 12 cubic metals to uniaxial loading. Phys. Rev. B, 58:6006–6018, 1998.

[34] M. Šob, L.G. Wang, and V. Vitek. Theoretical tensile stress in tungsten single crystals by full-potential first-principles calculations. Materials Science and Engineering: A, 234:1075 – 1078, 1997.

[35] The elk fp-lapw code. http://elk.sourceforge.net/, 2017.

[36] N. Nagasako, M. Jahnátek, R. Asahi, and J. Hafner. Anomalies in the response of V, Nb, and Ta to tensile and shear loading: Ab initio density functional theory calculations. Phys. Rev. B, 81:94108, 2010.

[37] A. Landa, J. Klepeis, P. Söderlind, I. Naumov, O. Velikokhatnyi, L. Vitos, and A. Ruban. Fermi surface nesting and pre-martensitic softening in v and Nb at high pressures. J. .Phys. Condens. Matter, 18:5079, 2006.

[38] M. I. Katsnelson, I. I. Naumov, and A. V. Trefilov. Singularities of the electronic structure and pre-martensitic anomalies of lattice properties in -phases of metals and alloys. Phase Transitions, 49:143–191, 1994.

[39] H. Olijnyk and W. B. Holzapfel. High-pressure structural phase transition in mg. Phys. Rev. B, 31:4682–4683, 1985.

[40] P. Lazar, M. Jahnátek, J. Hafner, N. Nagasako, R. Asahi, C. Blaas-Schenner, M. Stöhr, and R. Podloucky. Temperature-induced martensitic phase transitions in gum-metal approximants: First-principles investigations for Ti_3Nb. Phys. Rev. B, 84:054202, 2011.

[41] R.J. Talling, R.J. Dashwood, M. Jackson, and D. Dye. Compositional variability in gum metal. Scripta Materialia, 60:1000 – 1003, 2009.

[42] A Stukowski. Structure identification methods for atomistic simulations of crystalline materials. Modell. Sim. Mater. Sci. and Eng., 20:045021, 2012.

[43] A. Stukowski. Visualization and analysis of atomistic simulation data with ovito–the open visualization tool. Modell. Sim. Mater. Sci. and Eng., 18:015012, 2010.

[44] W.G. Burgers. On the process of transition of the cubic-body-centered modification into the hexagonal-close-packed modification of zirconium. Physica, 1:561 – 586, 1934.

[45] Y. Hanlumyuang, R. P. Sankaran, M. P. Sherburne, J. W. Morris, and D. C. Chrzan. Phonons and phase stability in Ti-V approximants to gum metal. Phys. Rev. B, 85:144108, 2012.

[46] C.J. Bradley and A.P. Cracknell. The Mathematical Theory of Symmetry in Solids. Oxford University Press, 2011.

[47] M. Tinkham. Group Theory and Quantum Mechanics. Dover, 1992.

[48] S.F. Pugh. Relations between the elastic moduli and the plastic properties of polycrystalline pure metals. The London, Edinburgh, and Dublin Philosophical Magazine and Journal of Science, 45:823–843, 1954.

[49] A.A Hashemi, A.D. Pelton, and J. B. Clark. Binary Alloy Phase Diagrams, 3:2444, 1990.

[50] M. Furui, H. Kitamura, H. Anada, and T. G. Langdon. Influence of preliminary extrusion conditions on the superplastic properties of a magnesium alloy processed by {ECAP}. Acta Mater., 55:1083 – 1091, 2007.

[51] M. Furui, C. Xu, T. Aida, M. Inoue, H. Anada, and T. G. Langdon. Improving the superplastic properties of a two-phase Gg–8% Li alloy through processing by {ECAP}. Mater. Sci. Eng. A, 410–411:439 – 442, 2005.

[52] H. Matsunoshita, K. Edalati, M. Furui, and Z. Horita. Ultrafine-grained magnesium–lithium alloy processed by high-pressure torsion: Low-temperature superplasticity and potential for hydroforming. Mater. Sci. Eng. A, 640:443 – 448, 2015.

[53] W.A. Counts, M. Friák, D. Raabe, and J. Neugebauer. Using ab initio calculations in designing bcc Mg–Li alloys for ultra-lightweight applications. Acta Mater., 57:69 – 76, 2009.

[54] I. Shin and E. A. Carter. First-principles simulations of plasticity in body-centered-cubic magnesium–lithium alloys. Acta Mater., 64:198 – 207, 2014.

[55] W. A. Counts, M. Friak, D. Raabe, and J. Neugebauer. Using ab initio calculations in designing bcc MgLi–X alloys for ultra-lightweight applications. Adv. Eng. Mater., 12:1198–1205, 2010.

[56] H.E. Cook and D. De Fontaine. On the elastic free energy of solid solutions—I. microscopic theory. Acta Metall., 17:915–924, 1969.

[57] C. B. Walker. X-ray study of lattice vibrations in aluminum. Phys. Rev., 103:547–557, 1956.

[58] D. De Fontaine. Mechanical instabilities in the bcc lattice and the β to ω phase transformation. Acta Metall., 18:275–279, 1970.

[59] K.-M. Ho, C. L. Fu, and B. N. Harmon. Vibrational frequencies via total-energy calculations. applications to transition metals. Phys. Rev. B, 29:1575–1587, 1984.

[60] M. Lax. Symmetry principles in solid state and molecular physics. John Wiley and Sons, 1974.

[61] A. van de Walle, P. Tiwary, M. de Jong, D.L. Olmsted, M. Asta, A. Dick, D. Shin, Y. Wang, L.-Q. Chen, and Z.-K. Liu. Efficient stochastic generation of special quasirandom structures. Calphad, 42:13–18, 2013.

[62] F. Tasnádi, M. Odén, and I. A. Abrikosov. Ab initio elastic tensor of Cubic $Ti_{0.5}Al_{0.5}N$ alloys: Dependence of elastic constants on size and shape of the supercell model and their convergence. Phys. Rev. B, 85:144112, 2012.

[63] M. de Jong, D. L. Olmsted, A. van de Walle, and M. Asta. First-principles study of the structural and elastic properties of rhenium-based transition-metal alloys. Phys. Rev. B, 86:224101, 2012.

[64] R.J. Talling, R.J. Dashwood, M. Jackson, and D. Dye. Compositional variability in gum metal. Scripta Mater., 60:1000 – 1003, 2009.

[65] I. S. Winter, M. Poschmann, T. Tsuru, and D. C. Chrzan. Dislocations near elastic instability in high-pressure body-centered-cubic magnesium. Phys. Rev. B, 95:064107, 2017.

[66] F. Milstein, J. Marschall, and H. E. Fang. Theoretical bcc ⇆ fcc transitions in metals via bifurcations under uniaxial load. Phys. Rev. Lett., 74:2977–2980, 1995.

[67] S.-H. Kim, H. Kim, and N. J. Kim. Brittle intermetallic compound makes ultrastrong low-density steel with large ductility. Nature, 518:77–79, 2015.

[68] W. Xiong and G. B. Olson. Integrated computational materials design for high-performance alloys. MRS Bull., 40:1035–1044, 2015.

[69] G. B. Olson and C. J. Kuehmann. Materials genomics: From CALPHAD to flight. Scripta Mater., 70:25–30, 2014.

[70] H.K.D.H. Bhadeshia. Computational design of advanced steels. Scripta Mater., 70:12–17, 2014.

[71] M. L. Cohen and A. Y. Liu. Science, 245:841, 1989.

[72] Amy Y. Liu and Marvin L. Cohen. Structural properties and electronic structure of low-compressibility materials: β-Si_3N_4 and hypothetical β-C_3N_4. Phys. Rev. B, 41:10727–10734, 1990.

[73] S. Veprek. The search for novel, superhard materials. J. Vac. Sci. Technol. A, 17:2401, 1999.

[74] S. Veprek. Recent search for new superhard materials: Go nano! J. Vac. Sci. Technol. A, 31:050822_1–050822_33, 2013.

[75] M. T. Yeung, R. Mohammadi, and R. B. Kaner. Ultraincompressible, Superhard Materials. Annu. Rev. Mater. Res., 46:465–485, 2016.

[76] D. B. Miracle, J. D. Miller, O. N. Senkov, C. Woodward, M. D. Uchic, and J. Tiley. Exploration and development of high entropy alloys for structural applications. Entropy, 16:494–525, 2014.

[77] M.-H. Tsai and J.-W. Yeh. High-Entropy Alloys: A Critical Review. Mater. Res. Let., 2:107–123, 2014.

[78] Z. Li, K. G. Pradeep, Y. Deng, D. Raabe, and C. C. Tasan. Metastable high-entropy dual-phase alloys overcome the strength–ductility trade-off. Nature, 534:227, 2016.

[79] E. Plancher, C.C. Tasan, S. Sandloebes, and D. Raabe. On dislocation involvement in Ti–Nb gum metal plasticity. Scripta Mater., 68:805–808, 2013.

[80] M.J. Lai, C.C. Tasan, and D. Raabe. Deformation mechanism of ω-enriched Ti–Nb-based gum metal: Dislocation channeling and deformation induced ω–β transformation. Acta Mater., 100:290–300, 2015.

[81] T. Furuta, S. Kuramoto, J. W. Morris, N. Nagasako, E. Withey, and D. C. Chrzan. The mechanism of strength and deformation in Gum Metal. Scripta Mater., 68:767-772, 2013.

[82] N. Nagasako, R. Asahi, D. Isheim, D. N. Seidman, S. Kuramoto, and T. Furuta. Microscopic study of gum-metal alloys: A role of trace oxygen for dislocation-free deformation. Acta Mater., 105:347–354, 2016.

[83] C. Baker. The shape-memory effect in a titanium-35 wt.-% niobium alloy. Met. Sci. J., 5(1):92–100, 1971.

[84] S. Kuramoto, N. Nagasako, T. Furuta, and Z. Horita. Strengthening the alloys with elastic softening in shear modulus C. J. Alloys Compd., 577:S147–S150, 2013.

[85] Liang Qi and D. C. Chrzan. Tuning ideal tensile strengths and intrinsic ductility of bcc refractory alloys. Phys. Rev. Lett., 112:1–5, 2014.

[86] A. Jain, S. P. Ong, G. Hautier, W. Chen, W. D. Richards, S. Dacek, S. Cholia, D. Gunter, D. Skinner, G. Ceder, et al. Commentary: The materials project: A materials genome approach to accelerating materials innovation. Apl. Mater., 1:011002, 2013.

[87] M. de Jong, W. Chen, T. Angsten, A. Jain, R. Notestine, A. Gamst, M. Sluiter, C. Krishna Ande, S. van der Zwaag, J. J. Plata, C. Toher, S. Curtarolo, G. Ceder, K. A. Persson, and M. Asta. Charting the complete elastic properties of inorganic crystalline compounds. Sci. Data, 2:1–13, 2015.

[88] K. Hanson and J. W. Morris Jr. Estimation of the critical resolved shear stress for dislocation glide through a random mixture of distinct obstacles. J. Appl. Phys., 46:2378–2383, 1975.

[89] A. N. Stroh. Dislocations and Cracks in Anisotropic Elasticity. Philos. Mag., 3:625–646, 1958.

[90] D. J. Bacon, D. M. Barnett, and R. O. Scattergood. Anisotropic continuum theory of lattice defects. Prog. Mater. Sci., 23:51–262, 1980.

[91] J.P. Hirth and J. Lothe. Theory of Dislocations. Krieger Publishing Company, 1982.

[92] K. Otsuka and X. Ren. Martensitic transformations in nonferrous shape memory alloys. Mater. Sci. Eng. A, 273-275:89–105, 1999.

[93] H. Y. Kim, S. Hashimoto, J. I. Kim, H. Hosoda, and S. Miyazaki. Mechanical properties and shape memory behavior of Ti-Nb alloys. Mater. Trans., 45:2443–2448, 2004.

[94] Y. Sutou, T. Omori, R. Kainuma, and K. Ishida. Ductile Cu–Al–Mn based shape memory alloys: general properties and applications. Mater. Sci. Technol., 24:896–901, 2008.

[95] K. Otsuka, K. Oda, Y. Ueno, M. Piao, T. Ueki, and H. Horikawa. The shape memory effect in a $Ti_{50}Pd_{50}$ alloy. Scripta Metall. Mater., 29:1355–1358, 1993.

[96] Y. Yamabe-Mitarai, R. Arockiakumar, A. Wadood, K. S. Suresh, T. Kitashima, T. Hara, M. Shimojo, W. Tasaki, M. Takahashi, S. Takahashi, et al. Ti (Pt, Pd, Au) based high temperature shape memory alloys. Mater. Today Proc., 2:S517–S522, 2015.

[97] T. W. Duerig, J. Albrecht, D. Richter, and P. Fischer. Formation and reversion of stress induced martensite in Ti-10V-2Fe-3Al. Acta Metall., 30:2161–2172, 1982.

[98] M. Methfessel and A. T. Paxton. High-precision sampling for brillouin-zone integration in metals. Phys. Rev. B, 40:3616–3621, 1989.

[99] A. Zunger, S.-H. Wei, L. G. Ferreira, and J. E. Bernard. Special quasirandom structures. Phys. Rev. Lett., 65:353–356, 1990.

[100] S.-H. Wei, L. G. Ferreira, J. E. Bernard, and A. Zunger. Electronic properties of random alloys: Special quasirandom structures. Phys. Rev. B, 42:9622–9649, 1990.

[101] S.-W. Chen, Y.-Y. Chuang, Y. A. Chang, and M. G. Chu. Calculation of phase diagrams and solidification paths of Al-rich Al- Li- Cu alloys. Metall. Trans. A, 22):2837–2848, 1991.

[102] F. Lanzini, R. Romero, and M. L. Castro. Influence of be addition on order–disorder transformations in β Cu–Al. Intermetallics, 16:1090–1094, 2008.

[103] Asm alloy phase diagram database. `http://mio.asminternational.org/apd/index.aspx`, 2016.

[104] L. H. Wen, H. C. Kou, J. S. Li, H. Chang, X. Y. Xue, and L. Zhou. Effect of aging temperature on microstructure and properties of AlCoCrCuFeNi high-entropy alloy. Intermetallics, 17:266–269, 2009.

[105] A. P. Prevarskii and R. V. Skolozdra. The Cr-Cu-Al system. Russian Metallurgy, 1:137–139, 1972.

[106] G. Ghosh and J. V. Humbeeck Aluminium-Copper-Zinc. Ternary Alloys, 5:92–112, 1992.

[107] R. Kainuma, S. Takahashi, and K. Ishida. Thermoelastic Martensite and Shape Memory Effect in Ductile Cu-AI-Mn Alloys. Metall. Mater. Trans. A, 27, 1996.

[108] R. Kainuma, J. J. Wang, T. Omori, Y. Sutou, and K. Ishida. Invar-type effect induced by cold-rolling deformation in shape memory alloys. Appl. Phys. Lett., 80:4348–4350, 2002.

[109] H. Y. Kim, L. Wei, S. Kobayashi, M. Tahara, and S. Miyazaki. Nanodomain structure and its effect on abnormal thermal expansion behavior of a Ti-23Nb-2Zr-0.7Ta-1.2O alloy. Acta Mater., 61:4874–4886, 2013.

[110] J. Pokluda and P. Šandera. Micromechanisms of Fracture and Fatigue: In a Multiscale Context. Springer, 2010.

[111] S. G. Corcoran, R. J. Colton, E. T. Lilleodden, and W. W. Gerberich. Anomalous plastic deformation at surfaces: Nanoindentation of gold single crystals. Phys. Rev. B, 55:16057–16060, 1997.

[112] M. M. Biener, J. Biener, A. M. Hodge, and A. V. Hamza. Dislocation nucleation in bcc Ta single crystals studied by nanoindentation. Phys. Rev. B, 76:1–6, 2007.

[113] C. A. Schuh, J. K. Mason, and A. C. Lund. Quantitative insight into dislocation nucleation from high-temperature nanoindentation experiments. Nat. Mater., 4:617–621, 2005.

[114] C. A. Schuh. Nanoindentation studies of materials. Mater. Today, 9:32–40, 2006.

[115] D.F. Bahr, D.E. Kramer, and W.W. Gerberich. Non-linear deformation mechanisms during nanoindentation. Acta Mater., 46:3605–3617, 1998.

[116] C.L Woodcock and D.F Bahr. Plastic zone evolution around small scale indentations. Scripta Mater., 43:783–788, 2000.

[117] J. Li, K. J. Van Vliet, T. Zhu, S. Yip, and S. Suresh. Atomistic mechanisms governing elastic limit and incipient plasticity in crystals. Nature, 418:307–10, 2002.

[118] M. L. Jokl, V. Vitek, and C. J. McMahon. A microscopic theory of brittle fracture in deformable solids: A relation between ideal work to fracture and plastic work. Acta Metall., 28:1479–1488, 1980.

[119] H. Huang and W. W. Gerberich. Crack-tip dislocation emission arrangements for equilibrium—II. Comparisons to analytical and computer simulation models. Acta Metall. Mater., 40:2873–2881, 1992.

[120] R. Hill and F. Milstein. Principles of stability analysis of ideal crystals. Phys. Rev. B, 15:3087–3096, 1977.

[121] F. Milstein and B. Farber. Theoretical fcc-bcc transition under [100] tensile loading. Phys. Rev. Lett., 44:277–280, 1980.

[122] T. Li, J. W. Morris, and D. C. Chrzan. Ideal tensile strength of $B2$ transition-metal aluminides. Phys. Rev. B, 70:054107, 2004.

[123] J. Frenkel. Zur Theorie der Elastizitätsgrenze und der Festigkeit kristallinischer Körper. Z. Phys., 37:572–609, 1926.

[124] X. Li, S. Schönecker, J. Zhao, B. Johansson, and L. Vitos. Ideal strength of random alloys from first principles. Phys. Rev. B, 87:214203 2013.

[125] C. Jiang and B. P. Uberuaga. Efficient ab initio modeling of random multicomponent alloys. Phys. Rev. Lett., 116:105501, 2016.

[126] H. Wang and M. Li. Ab initio calculations of second-, third-, and fourth-order elastic constants for single crystals. Phys. Rev. B, 79:1–10, 2009.

[127] F. Birch. Finite elastic strain of cubic crystals. Phys. Rev., 71:809–824, 1947.

[128] M. de Jong, L. Qi, D. L. Olmsted, A. van de Walle, and M. Asta. Calculations of planar defect energies in substitutional alloys using the special-quasirandom-structure approach. Phys. Rev. B, 93:094101, 2016.

[129] A. van de Walle, M. Asta, and G. Ceder. The alloy theoretic automated toolkit: A user guide. Calphad, 26:539–553, 2002.

[130] A. van de Walle. Multicomponent multisublattice alloys, nonconfigurational entropy and other additions to the alloy theoretic automated toolkit. Calphad, 33:266–278, 2009.

[131] T. Li, J. W. Morris, and D. C. Chrzan. Ab initio study of the ideal shear strength and elastic deformation behaviors of B2 FeAl and NiAl. Phys. Rev. B, 73:024105, 2006.

[132] V. A. Lubarda. New estimates of the third-order elastic constants for isotropic aggregates of cubic crystals. J. Mech. Phys. of Solid, 45:471 – 490, 1997.

[133] H. Wang and M. Li. Ab initio calculations of second-, third-, and fourth-order elastic constants for single crystals. Phys. Rev. B, 79:224102, 2009.

[134] M. Cerny, M. Šob, J. Pokluda, and P. Šandera. Ab initio calculations of ideal tensile strength and mechanical stability in copper. J. Phy. Condens. Matter, 16:1045, 2004.

[135] M. Černý and J. Pokluda. Ideal tensile strength of cubic crystals under superimposed transverse biaxial stresses from first principles. Phys. Rev. B, 82:174106, 2010.